

The Pennsylvania State University
The Graduate School
College of Engineering

NUMERICAL ANALYSIS OF
FREQUENCY SELECTIVE SURFACES

A Thesis in
Electrical Engineering
by
Nikhil Mehta

© 2010 Nikhil Mehta

Submitted in Partial Fulfillment
of the Requirements
for the Degree of

Master of Science

August 2010

The thesis of Nikhil Mehta was reviewed and approved* by the following:

Raj Mittra

Professor of Electrical Engineering

Thesis Adviser

James Breakall

Professor of Electrical Engineering

Kenneth Jenkins

Professor of Electrical Engineering

Head of the Department of Electrical Engineering

*Signatures are on file in the Graduate School.

Abstract

The Method of Moments (MoM) is a numerical technique for solving the integro-differential field equations arising in computational electromagnetics (CEM) has evolved into a versatile and mature computational tool for solving a large variety of scattering problems involving arbitrary structures. However, the MoM requires knowledge of the Green's function for the medium in which the scatterer is present, and special treatment is necessary to tackle the singularity issues that arise in the integral equation based on this Green's function. To address these concerns, we introduce a new technique called the Dipole Moment method (DM) which uses the knowledge of the induced dipole moments in a small sphere under the influence of a plane wave. Although this method follows the matrix-based approach used in MoM to solve for the unknown currents induced on an object, it avoids the direct use of the Green's function and hence is free from the singularity issues. The DM utilizes relatively large number of unknowns to solve the matrix equation compared to the conventional MoM. In order to improve the numerical efficiency of the DM method, we introduce a set of high-level macro basis functions, referred to herein as the Characteristic Basis Functions (CBFs). The use of CBFs leads to a well-conditioned interaction matrix whose size is substantially smaller than the size of the matrix required in DM or in conventional MoM for accurate solution. In particular, we introduce a numerically efficient technique based on a combination of the DM and CBFs to analyze doubly infinite periodic structures, also called as Frequency Selective Surfaces (FSSs). We also develop a new method based on the reciprocity principle, to calculate the reflection coefficient of the FSS. This method circumvents the need to integrate the current distribution on the FSS to find scattered far-fields from the array. We validate the numerical technique introduced in this thesis by comparing our results for the reflection coefficient of the FSS with those obtained from commercially available MoM-based codes, and show that it is able to analyze planar, non-planar and multi-layered FSSs.

Table of Contents

List of Figures	vi
Acknowledgements	viii
1 Dipole Moment Formulation	1
1.1 A summary of Method of Moments	1
1.2 Dipole Moment Formulation	5
1.3 Numerical Results	11
1.4 Conclusions	15
2 Macro Basis Functions	17
2.1 Introduction	17
2.2 Macro Basis Functions	18
2.3 Characteristic Basis Functions	19
2.4 Procedure for generating Characteristic Basis Functions	20
2.5 CBFs for some standard PEC wire structures	22
2.6 Conclusion	26
3 Frequency Selective Surfaces	29
3.1 Introduction	29
3.2 Formulation	31

3.3	Reflection Coefficient	36
3.4	Numerical Results	43
3.4.1	Planar Frequency Selective Screens	45
3.4.2	Non-planar Frequency Selective Arrays	52
3.5	Conclusion	56
4	Conclusions and Future Work	58
	Bibliography	60

List of Figures

1.1	Illustration of Conventional Method of Moments	3
1.2	Dipole Moments induced in a small sphere by an incident plane wave . . .	6
1.3	Illustration of Dipole Moment-based formulation	8
1.4	Method for assigning direction to the dipole-moments	9
1.5	Induced current distribution on small PEC wire	12
1.6	Induced current distribution on PEC bent-wire structure	13
1.7	Induced current distribution on PEC turnstile structure	14
1.8	Induced current distribution on Half-Wave Dipole	15
2.1	Use of Macro Basis Functions to reduce number of unknowns in DM	18
2.2	Current Distribution on PEC wire by using DM with MBF	19
2.3	Illustration of the procedure to generate Characteristic Basis Functions . .	21
2.4	CBFs for the inner loop of a double loop element	23
2.5	CBFs for the outer loop of a double loop element	24
2.6	CBFs for the inner loop of a double split loop element	25
2.7	CBFs for the outer loop of a double split loop element	26
2.8	CBFs for the loop of a DNG meta-material element	27
2.9	CBFs for the wire of a DNG meta-material element	28
3.1	Frequency Selective Surface	29

3.2	Geometry of FSS of dipole element	32
3.3	34
3.4	Use of moving average filter to extrapolate asymptotic value of current . .	35
3.5	Illustration of Reciprocity Principle	37
3.6	Application of Reciprocity to find equivalent expression for Reflection Coefficient	38
3.7	Projected area of the unit cell along the direction of incident wave-vector .	42
3.8	Reflection Coefficient of Dipole FSS	43
3.9	FSS made of Square Loop	46
3.10	R of Square Loop FSS with cell size = 0.5λ	47
3.11	R of Square Loop FSS with cell size = 0.7λ	48
3.12	FSS made of Split Square Loop as its element	49
3.13	R of Split Square Loop FSS, cell size = 0.5λ & $E^{inc} \perp \text{split}$	49
3.14	R of Split Square Loop FSS, cell size = 0.7λ & $E^{inc} \perp \text{split}$	50
3.15	R of Split Square Loop FSS, cell size = 0.5λ & $E^{inc} \parallel \text{split}$	50
3.16	R of Split Square Loop FSS, cell size = 0.7λ & $E^{inc} \parallel \text{split}$	50
3.17	Results for FSS consisting of tripole as an element	51
3.18	Typical geometry of non-planar FSS	53
3.19	R of FSS of square loop titled out-of-plane by 45°	53
3.20	Typical geometry of non-planar FSS	54
3.21	R of FSS of square loop titled out-of-plane by 90°	55
3.22	Effect on current distribution on FSS by tilting a square loop out-of-plane	56

Acknowledgement

My mom (Aai) and dad (Baba) have been my pillars of support throughout my formative years. It is to them that I owe the strength and conviction to stand by my decisions each day.

The opportunity to work under the able guidance of my advisor Dr. Raj Mittra has taught me that it demands religious dedication and perseverance to generate a body of work of the highest calibre. He is not only an established authority in the domain of Electromagnetics, but also an excellent teacher because of his clarity in thoughts, which has enhanced my understanding of the subject. I hope that the agility of his mind and the rigour in his approach towards his work will forever serve both as a reference and an inspiration to help shape my career, and I humbly acknowledge his contribution to my thesis.

I am grateful to my colleagues in the Electromagnetics Communication Laboratory; in particular Kadappan for the many discussions over coffee, and the time-critical help whenever needed, Jonathan, Kyungho Hoo and Arash for answering the numerous questions and the insightful technical discussions, and Dr. Wenhau Yu, Xialong (Bob) Yang and Dr. Neng-Tien Huang for helping me with the use of the numerical codes. Finally, I appreciate Dr. James Breakall who took time out of his schedule and agreed to peruse my work at a short notice.

1. Dipole Moment Formulation

1.1 A summary of Method of Moments

Method of Moments (MoM)[1] is a computational technique which begins by replacing a given object, which is immersed in an electromagnetic field, with the induced conduction current \mathbf{J}_s . We can compute the electric field generated by the induced current by expressing it in terms of the vector potential \mathbf{A} as:

$$\mathbf{E} = -j\omega\mathbf{A} - \frac{j}{\omega\mu\epsilon}\nabla(\nabla \cdot \mathbf{A}), \quad (1.1a)$$

where we have made use of the Lorenz gauge: $\phi = j/\omega\mu\epsilon(\nabla \cdot \mathbf{A})$ and where \mathbf{A} is related to the current \mathbf{J}_s via the equation

$$\mathbf{A}(r) = \frac{\mu}{4\pi} \iint_S \mathbf{J}_s(r') \frac{e^{-jk(\mathbf{r}-\mathbf{r}')}}{|\mathbf{r}-\mathbf{r}'|} ds'. \quad (1.1b)$$

We identify the free space Green's function

$$G(r, r') = \frac{e^{-jk(r-r')}}{(r-r')}$$

in (1.1b). This current is expanded in a set of suitable basis functions $\mathbf{b}_n(\mathbf{r}')$ with unknown weights w_n , as:

$$\mathbf{J}_s(\mathbf{r}') = \sum_{n=1}^N w_n \mathbf{b}_n(\mathbf{r}'). \quad (1.2)$$

The choice of these basis functions is an important factor in determining the accuracy and stability of the numerical solution[2]. Ideally, the basis functions are chosen such that they can capture the unknown current distribution without introducing numerical artifacts. Next we impose the boundary condition on the surface of the perfect electric conducting (PEC) scatterer that the total tangential electric field be zero:

$$\mathbf{E}_{\text{tan}}^{\text{total}} = \mathbf{E}_{\text{tan}}^{\text{inc}} + \mathbf{E}_{\text{tan}}^{\text{scat}} = 0. \quad (1.3)$$

Using (1.1a) and the boundary condition (1.3), we can form the general Electric Field Integral Equation (EFIE), which reads[3]:

$$\frac{j\eta}{k} \left\{ k^2 \iint_S \mathbf{J}_s(r') G(r_s, r') ds' + \nabla \iint_S \nabla' \cdot \mathbf{J}_s(r') G(r_s, r') ds' \right\} = \mathbf{E}^i(r_s). \quad (1.4)$$

Eqn (1.4) forms the basic starting point for the MoM formulation. At this stage, we substitute the expanded current of (1.2) in (1.4). After making suitable assumptions pertinent to the geometry (see for eg citebalanis), and by applying the boundary conditions at N points along the surface, we form a system of linear equation in the n unknown weights w_n . Typically, the Galerkin procedure is used wherein both the incident field \mathbf{E}^i and field scattered by induced current are weighted by using the same set of basis functions. This is equivalent to matching the boundary conditions in an ‘average’ sense over the surface. It helps to reduce the residual and to speed up the convergence of the numerical solution[4]. As an example of the EFIE, we mention the widely used Pocklington Integral Equation[5] for a thin wire of radius a and length l oriented along \hat{z} , as shown in Fig.1.1.

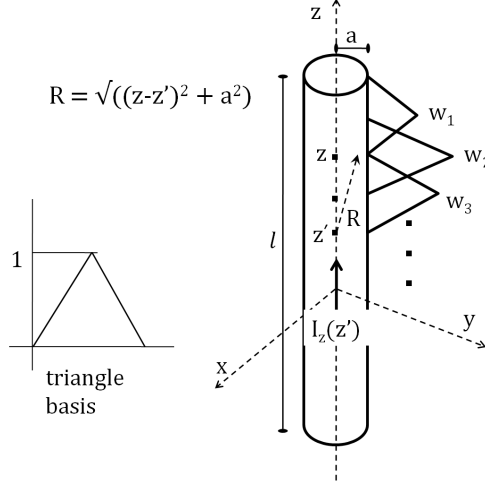


Figure 1.1: Expansion of the unknown induced current on a wire using triangle basis functions. The weights of the expansion functions are w_i . The wire is assumed to be thin, $a \ll \lambda$. Current is assumed to flow along the axis of the wire, and not on its surface, to avoid the singularity in Green's function when evaluating the self term of the Z matrix.

$$\int_{-l/2}^{+l/2} I_z(z') \left[\left(\frac{\partial^2}{\partial z^2} + k^2 \right) G(z, z') \right] dz' = -j\omega\epsilon E_z^i(\rho = a) \quad (1.5)$$

where \mathbf{k} is wave-vector of the incident wave and ϵ is the permittivity of the medium. If we assume that the wire is very thin ($a \ll \lambda$), and that the current along the wire is uniform around its circumference, i.e. $\mathbf{J}_z = \frac{I_z(z')}{2\pi a}$, then this equation can be expressed in a convenient form as[6]

$$\frac{1}{4\pi} \int_{-l/2}^{l/2} I_z(z') \frac{G(z, z')}{R^4} [(1 + jkR)(2R^2 - 3a^2) + (kaR)^2] dz' = -j\omega\epsilon E_z^i(\rho = a). \quad (1.6)$$

where $R = \sqrt{a^2 + (z - z')^2}$. If we treat the integration in (1.6) as a linear operator \mathfrak{L} , we get the system of linear equations

$$\sum_{n=1}^N w_n \mathfrak{L}(b_n, b_m) = -h_m, \quad m = 1, 2, \dots, N. \quad (1.7)$$

Here, the operator \mathfrak{L} involves the operations of both evaluating the fields of basis function b_n , as well weighting them by basis function b_m ; and h_m is the tangential component of

\mathbf{E}^i weighted by b_m . Finally, (1.7) can be written in the more familiar matrix form, as

$$[Z_{mn}][I_n] = [V_m], \quad (1.8)$$

where, $Z_{mn} = \mathfrak{L}(b_n, b_m)$; $I_n = w_n$; and $V_m = -h_m$. The solution to the problem can be written as

$$[I_n] = [Z_{mn}]^{-1}[V_m].$$

The MoM solution based on the EFIE, described above, inherently suffers from the singularity issue encountered while evaluating the diagonal terms in system matrix $[Z_{mn}]$. This is because the diagonal entries, i.e., the self terms, which describe the interaction of a basis function with itself, require that the boundary condition be applied at the location of the current source, and this leads to a singular behavior when evaluating the Green's function. However, numerical integration through a singularity is computationally expensive, and may yield incorrect results unless handled carefully. Analytical techniques for singularity extraction have been proposed to overcome the numerical integration in the source region.[7, 8, 9]. Typically, for wire-type structure, the problem is avoided by assuming that the current flows along the wire axis, instead of on its surface, so that $R \neq 0$ for the self term *.

Another issue faced by conventional MoM is that it breaks down at low frequencies. From (1.1a), we note that the contribution of scalar potential term $-\nabla\phi$ dominates significantly over that from the vector potential \mathbf{A} when the frequency is low, which leads to inaccuracy in the numerical solution. This is true, in general, for electrically small structures as well as for near-field calculations. Thus, even the terms adjacent to the self term

*A formal way to overcome singularity is to split the volume of integral in (1.1b) by a fictitious sphere of finite small radius a over which the current \mathbf{J} is well behaved and retardation is insignificant. Using a Taylor series expansion for the current within this sphere and letting $a \rightarrow 0$ we can get the desired non-singular expression. This method has been described in [10],§.1.7

can place a heavy burden on processor time and memory. To circumvent these problems, we introduce in Sec.1.2 a new method that solves for the unknown current based on the induced dipole moments of small scatterers.

1.2 Dipole Moment Formulation

The Dipole Moment (DM) approach is a method based on the MoM paradigm to solve the scattering problem at hand without involving the EFIE directly as in the conventional MoM[11]. In this method we use the induced dipole moments of a small sphere to model the current flowing through a wire PEC structure. We begin by considering an x -polarized, plane wave traveling along the \hat{a}_z direction whose \mathbf{E} - field is expressed as $\mathbf{E}^i = \hat{a}_x E_0 e^{-jkz}$. We let this wave be incident on a sphere of radius a located at origin, as shown in Fig.1.2. Following Harrington[12], we can show that in the limit $ka \rightarrow 0$, the scattered fields are given by

$$\lim_{ka \rightarrow 0} E_\theta^s = E_0 \frac{e^{-jkr}}{kr} (ka)^3 \cos(\phi) \left(\cos \theta - \frac{1}{2} \right) \quad (1.9a)$$

$$\lim_{ka \rightarrow 0} E_\phi^s = E_0 \frac{e^{-jkr}}{kr} (ka)^3 \sin(\phi) \left(\frac{1}{2} \cos \theta - 1 \right). \quad (1.9b)$$

These fields are the same as from an equivalent x -directed electric dipole moment (EDM) and y -directed magnetic dipole moment (MDM) given by,

$$\begin{aligned} \mathbf{\Pi} &= E_0 \frac{4\pi j}{\eta k^2} (ka)^3 \hat{a}_x \\ \mathbf{Kl} &= E_0 \frac{2\pi}{jk^2} (ka)^3 \hat{a}_y. \end{aligned} \quad (1.10)$$

At this point, we observe that:

- (i) in general, a linear combination of these dipole moments can be used to generate

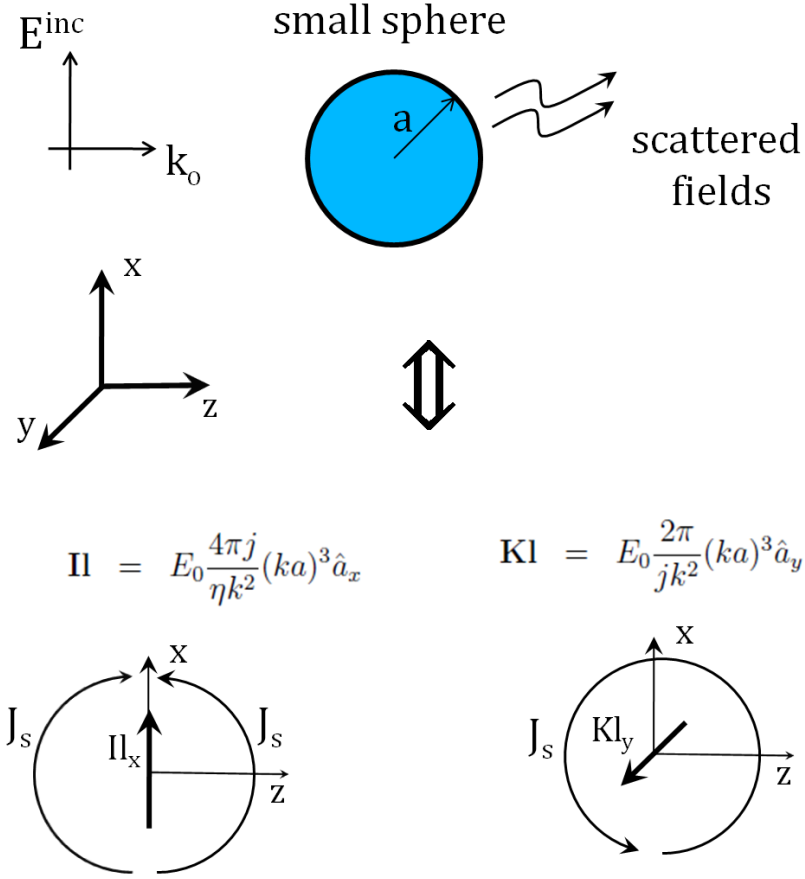


Figure 1.2: Electric dipole moment $\mathbf{\Pi}$ and magnetic dipole moment \mathbf{KI} induced in a small sphere of radius a which is illuminated by an incident plane wave, E^{inc} . For a PEC sphere, only $\mathbf{\Pi}$ is significant.

the scattered fields from any small body;

(ii) typically, for a PEC scatterer, only the electric dipole moment is significant;

(iii) it can be shown (by considering the small argument expressions for spherical Bessel and Hankel functions and their derivatives,[13] that the expressions in (1.9) are valid everywhere outside the sphere, even in the near-field, all the way up-to the surface of the sphere.

It is well known that the fields radiated by a small current dipole of strength $\mathbf{\Pi} = Il\hat{a}_z$ are given as

$$E_\theta(r) = j(I_0 l) \frac{\eta k^2 \sin \theta}{4\pi} \left[\frac{1}{kr} + \frac{1}{j(kr)^2} - \frac{1}{(kr)^3} \right] e^{-jkr} \quad (1.11a)$$

$$E_r(r) = (I_0 l) \frac{\eta k^2 \cos \theta}{2\pi} \left[\frac{1}{(kr)^2} + \frac{1}{j(kr)^3} \right] e^{-jkr} \quad (1.11b)$$

$$H_\phi(r) = j(I_0 l) \frac{k^2 \sin \theta}{4\pi} \left[\frac{1}{kr} + \frac{1}{j(kr)^2} \right] e^{-jkr}. \quad (1.11c)$$

By substituting the EDM of the small sphere (1.10) in (1.11), the fields radiated by the induced dipole moment can be expressed in terms of the incident field E_0 as

$$E_\theta^{dm}(r) = -E_0 \sin \theta (ka)^3 \left[\frac{1}{kr} + \frac{1}{j(kr)^2} - \frac{1}{(kr)^3} \right] e^{-jkr} \quad (1.12a)$$

$$E_r^{dm}(r) = j2E_0 \cos \theta (ka)^3 \left[\frac{1}{(kr)^2} + \frac{1}{j(kr)^3} \right] e^{-jkr} \quad (1.12b)$$

$$H_\phi^{dm}(r) = -\frac{E_0}{\eta} \sin \theta (ka)^3 \left[\frac{1}{kr} + \frac{1}{j(kr)^2} \right] e^{-jkr}. \quad (1.12c)$$

The next step in the DM formulation is to replace the structure by a string of spheres, as shown in Fig.1.3. The unknown current induced on the structure is expressed in terms of the induced dipole moment in each sphere. The effective field incident on each sphere is a combination of the incident plane wave excitation and the fields scattered by every other sphere. Next we impose the boundary condition on the surface of each sphere by matching the scattered fields, given by (1.12), to the given incident field E^i , to set up a system of simultaneous linear equations to solve for the induced EDMs. Next, we apply the standard spherical-to-cartesian coordinate transformation to the fields in (1.12) to obtain the field components E_x^{dm} , E_y^{dm} and E_z^{dm} . Using these, we can find the tangential field component of the effective field, E_{tan}^{dm} radiated by each dipole moment. The resulting

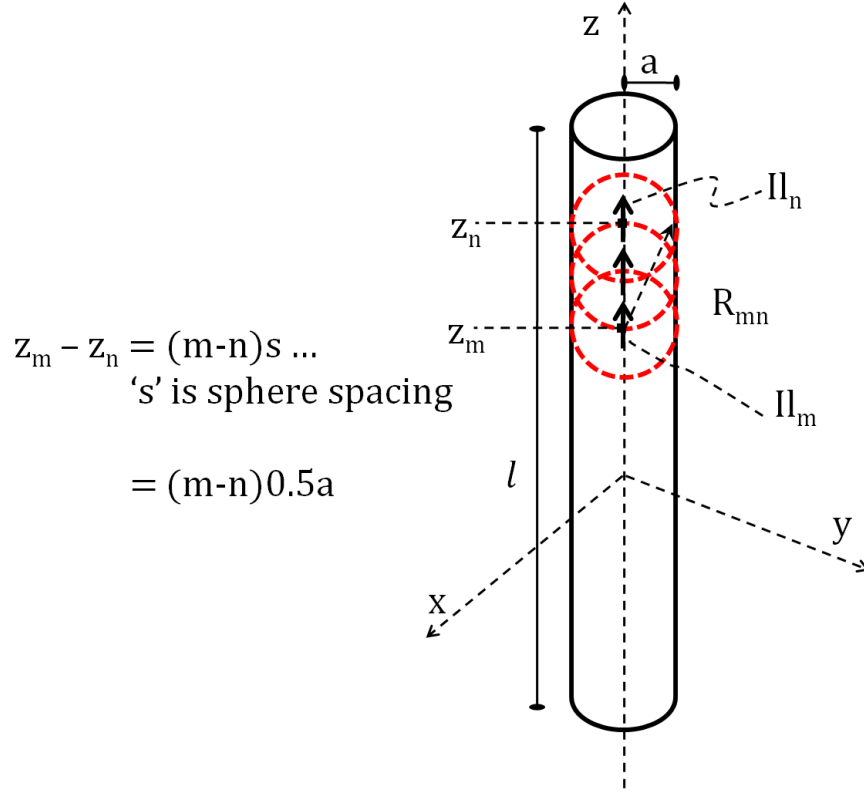


Figure 1.3: Illustration of the use of a string of dipole moments to model the induced current on a PEC wire of radius a and length l . The radii of spheres is a . The EDM, Il_i , induced in each sphere are the unknowns. The spacing between centers of adjacent spheres is $s = 0.5a$.

system of linear equations reads,

$$\sum_{n=1}^N E^n E_{tan}^{dm}(R_{mn}) = -E_{tan}^i|_m \quad m = 1, 2, \dots N, \quad (1.13)$$

where E^n are the unknowns; $E_{tan}^i|_m$ is the tangential component of the incident plane wave at the location of the m^{th} sphere; and R_{mn} is the distance between the n^{th} dipole moment and the location of the m^{th} sphere. Once we have solved for E^n , we use (1.10) to derive the induced dipole moment Il_n and hence the current at the location of each sphere. However, to do this we need to assign a 'direction' to each dipole moment. Since the cascaded set of spheres must describe the direction of flow of the continuous conduction

current in the PEC structure, we assume that the dipole moments are aligned along its axis. We write this as: $\mathbf{\Pi}_i = Il_x\hat{x} + Il_y\hat{y} + Il_z\hat{z}$. This concept is illustrated in Fig.1.4. In short, the component dipole moments of a sphere are weighted by the direction cosines of a line connecting the center of the sphere to that of the adjacent sphere.

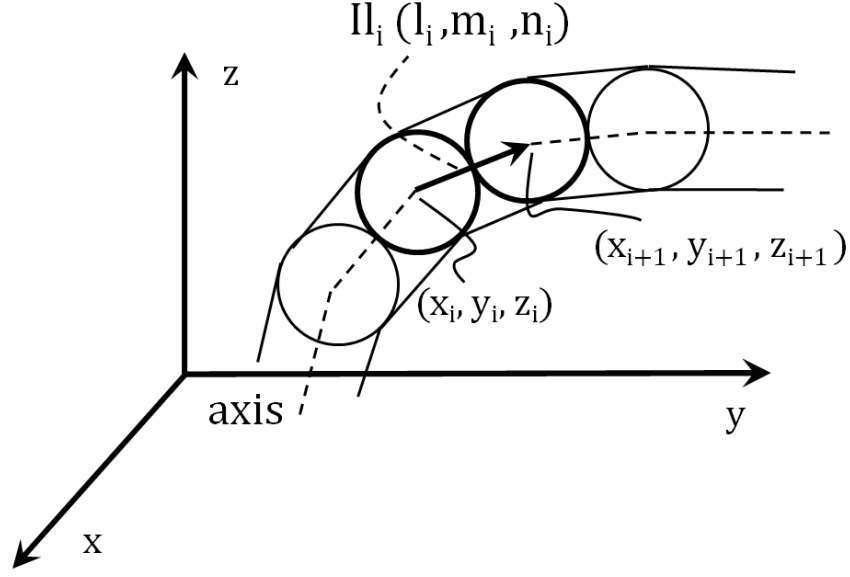


Figure 1.4: Illustration of the method to assign direction to each dipole-moment. (x_i, y_i, z_i) and $(x_{i+1}, y_{i+1}, z_{i+1})$ denote the centers of i^{th} and $(i+1)^{th}$ dipole moment respectively. The triplet (l_i, m_i, n_i) defines the direction cosines of the unit vector along the wire-axis at the location of the i^{th} sphere.

We would like to comment on some salutary features of the dipole moment expressions given in (1.10). We note that the EFIE in (1.4) relates the unknown current to its field via a convolution integral involving the Green's function and the basis function, and that the numerical integration employed to calculate the diagonal entries in $[Z_{mn}]$ can be computationally intensive owing to the singularity in self term. In contrast, the Electric Dipole Moment (EDM) Il , given in (1.10), is related to the incident field simply by a constant, which depends on the frequency and the radius of sphere. In this approach, we bypass the integration step and hence the attendant singularity problems. In fact,

we choose the radius of the sphere to be that of the wire being modeled. In this sense, the sphere also has a physical interpretation in that it may be viewed as a basic building block of the geometry of the object being analyzed.

A key observation is that the dipole moment $Il = O(a^3)$. If we consider the interaction of a dipole moment with itself and with those located in its vicinity, the electric fields from (1.11) are $E = O(1/r^3)$. Thus, no matter how thin a wire is, the self term of the DM matrix will always be $O(1)$, and this is the same as the order of the incident plane wave. This can be seen from the equations below,

$$\lim_{kr \rightarrow 0} E_r^{dm}(r) = 2E_0 \left(\frac{a}{r}\right)^3 \cos \theta \quad (1.14a)$$

$$\lim_{kr \rightarrow 0} E_\theta^{dm}(r) = E_0 \left(\frac{a}{r}\right)^3 \sin \theta. \quad (1.14b)$$

This is in contrast to MoM, where the order of the self term can be $O(1e4 \sim 1e5)$. We can identify a^3 as being related to the ‘form factor’ of the small sphere. In principle, we could choose a different shape for the building block instead of the sphere, but its dipole moment may not be as conveniently available as it is for the sphere. The choice of the sphere as the building block is significant in this context.

Earlier we noted in Sec.1.1 that the MoM formulation breaks down at low frequencies due to the disparity in the relative contributions of the scalar potential ϕ and the vector potential \mathbf{A} . However, we note from (1.14), that the near fields generated via the DM method are independent of frequency. This means that in applications where we are only interested in the near fields, the DM formulation can be used all the way down to DC, without requiring any special treatments. An example of such an application is the hybridization of a frequency domain method such as the DM with a time domain method like the Finite Difference Time Domain (FDTD) algorithm. It is well known that the

FDTD method requires a fine mesh to discretize scatterers that are smaller in size than the typical cell size of $\lambda/20$. However, instead of discretizing the small scatterer finely, we can use the DM approach to solve for the current on it, and find its radiated fields on the boundaries of the FDTD cell. These fields may then be used as the input to the subsequent iteration of the leapfrog FDTD algorithm[14]. This obviates the need to use a fine mesh, and makes such a hybrid scheme attractive for solving problems that have multi-scale character. Such a multi-frequency analysis has been demonstrated as a proof of concept in citejonathan. Of course, we reiterate the fact that such a hybrid approach is valid to analyze electrically small scatterers embedded in a background medium.

Finally, since we see from (1.10) that the field generated by the dipole moment is simply a scalar multiple of the incident field, the ‘sphere’ may be viewed as playing that role of a mental construct to aid the understanding of DM formulation. In fact, we we may view the use of each individual dipole moment as a way to discretize the current distribution on the wire. We have found[15] that for PEC wires, a spacing of $\approx 0.5a$ (a = wire radius), between the location of adjacent dipole moments along the wire yields the correct solution. This is shown in Fig.1.3. With this discussion in mind, we next proceed to show some results derived by using the DM approach.

1.3 Numerical Results

In this section, we present a few illustrative examples that demonstrate the accuracy of the dipole moment method by comparing the results for the current distributions on some typical wire geometries, obtained by using the MoM and the DM techniques. We have used the MoM code “Numerical Electromagnetic Code” (NEC) for the purpose of comparison. We begin by considering a small PEC wire of length $\lambda/10$ and radius of

$\lambda/100$ oriented along \hat{a}_z which is illuminated by a \hat{a}_z -polarized plane wave, travelling along the \hat{a}_y direction, as shown in Fig.1.5 We note from this figure that the comparison

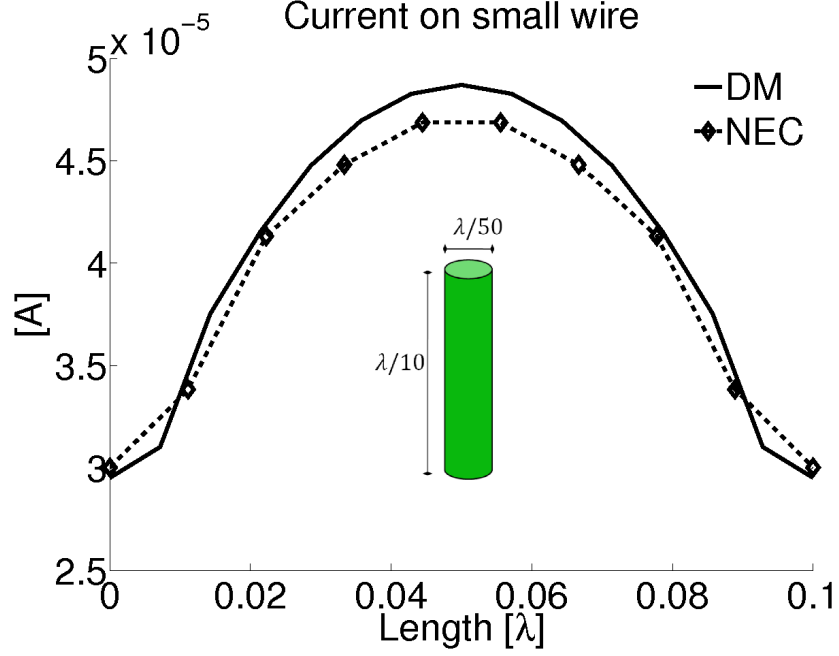


Figure 1.5: Comparison of the magnitude of current distribution on small PEC wire of length $\lambda/10$ and radius $\lambda/100$. Incident plane wave is polarized along the length of the wire.

between the MoM results, generated by the NEC code and the DM approach compare very favorably with each other.

For the next example, we consider a bent-wire geometry, which is shown in the inset in Fig. 1.6. The arm-lengths of the two arms of the PEC bent-wire are $\lambda/10$. The wire has a radius of $\lambda/100$. For the sake of demonstration, we have considered an included angle of $\pi/2$ between the two arms. We note that the induced currents computed using DM approach agree with the MoM results. The \hat{a}_z -polarized incident wave induces a stronger current in the \hat{a}_z -directed arm. The current distribution at the bend is continuous as it flows into the \hat{a}_y -directed arm.

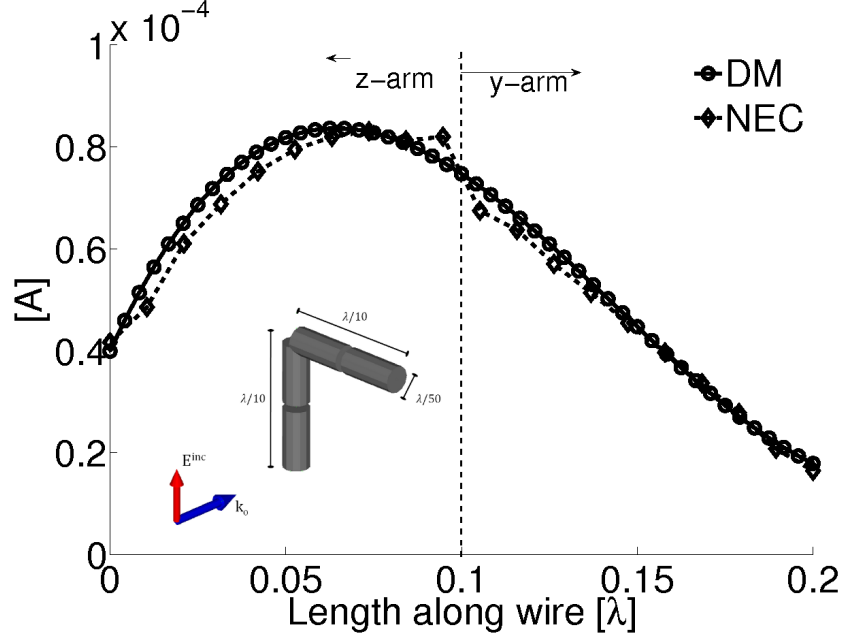


Figure 1.6: Comparison of the magnitude of current distribution on a PEC bent-wire structure. Length of each arm of the bent-wire is $\lambda/10$, and the radius is $\lambda/100$. The incident electric field is polarized along the vertical arm.

In the next example, we consider a turnstile structure, which has three mutually perpendicular arms, oriented along each of the three coordinate axes. The arms meet at a junction where the current can flow along multiple paths, such that Kirchoff's current law is satisfied. As before, each arm is $\lambda/10$ long and has a radius of $\lambda/100$. The level of current induced in each arm depends on the incident excitation. As shown in Fig.1.7(a)–(c), we consider different incident plane waves and compare the induced current distributions along the turnstile. In particular, Fig.1.7(c) shows the current distribution when the incident field has its wave-vector k_0 given by the angles $(\theta = \pi/4, \phi = \pi/4)$, and moreover, the electric field is polarized along an angle $\delta = \pi/4$ measured from the unit vector \hat{a}_θ . Thus all the three cartesian components of the incident electric field excite the turnstile structure, and the excitations are all of different strengths. From Fig.1.7, we see that the agreement between the current distributions obtained by using the DM and MoM is excellent for this case, as for the other cases considered in that figure. There are some differences between the NEC and DM results for the currents near the corners because the

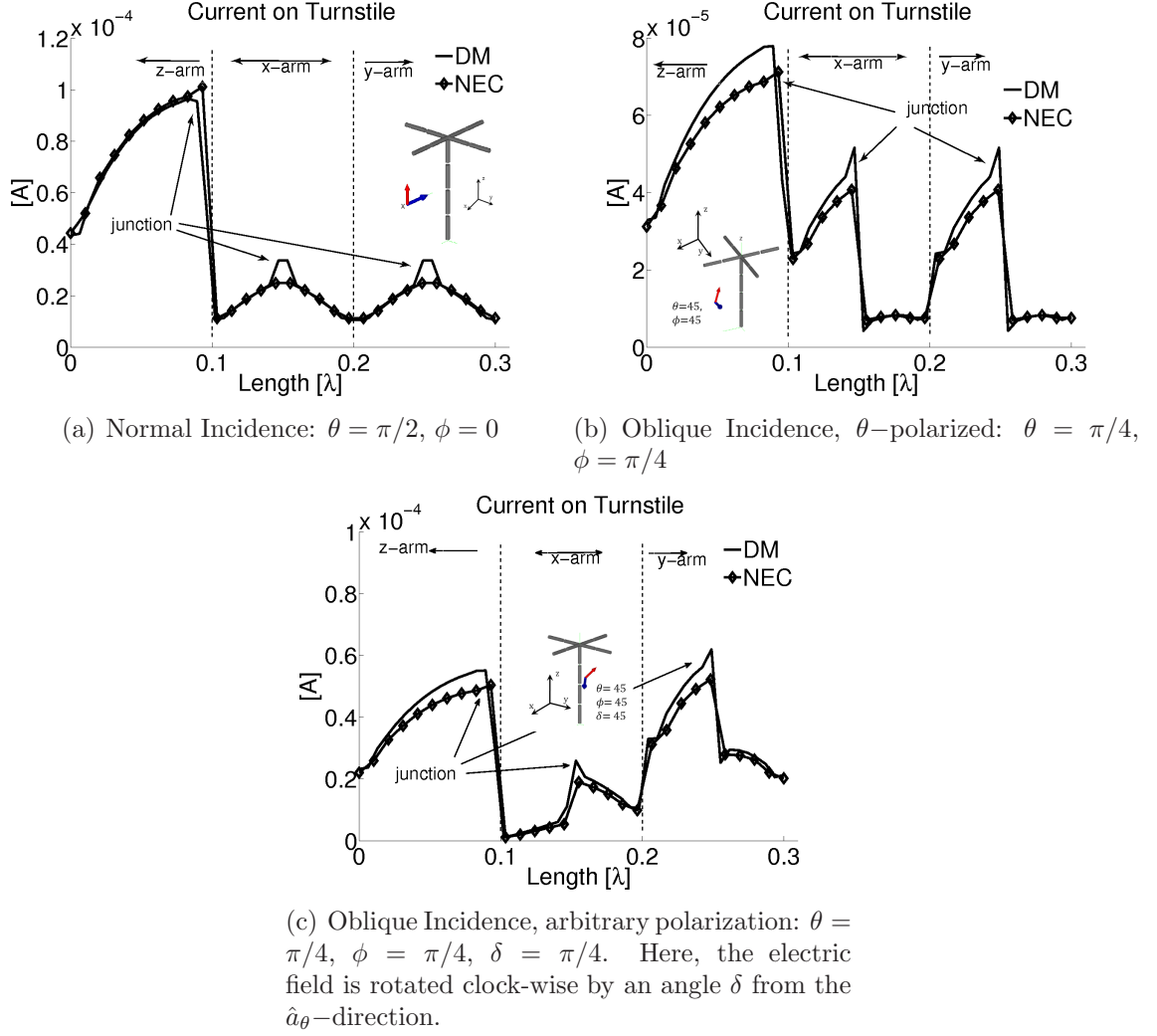


Figure 1.7: Comparison of the magnitude of current distribution on PEC turnstile structure illuminated by a plane wave. Each arm of turnstile is $\lambda/10$ long and has radius of $\lambda/100$.

adjacent dipole moments are located nearer as we turn around the junction than along the length. This, in turn, introduces a numerical artifact in the matrix, which causes the current to have a slight discontinuity near the junction where the three arms meet.

Finally, to show that the DM approach can be used even for structures whose size is comparable to λ , we compare the induced currents on a simple half-wave dipole, whose radius is $\lambda/100$. The result is shown in Fig.1.8.

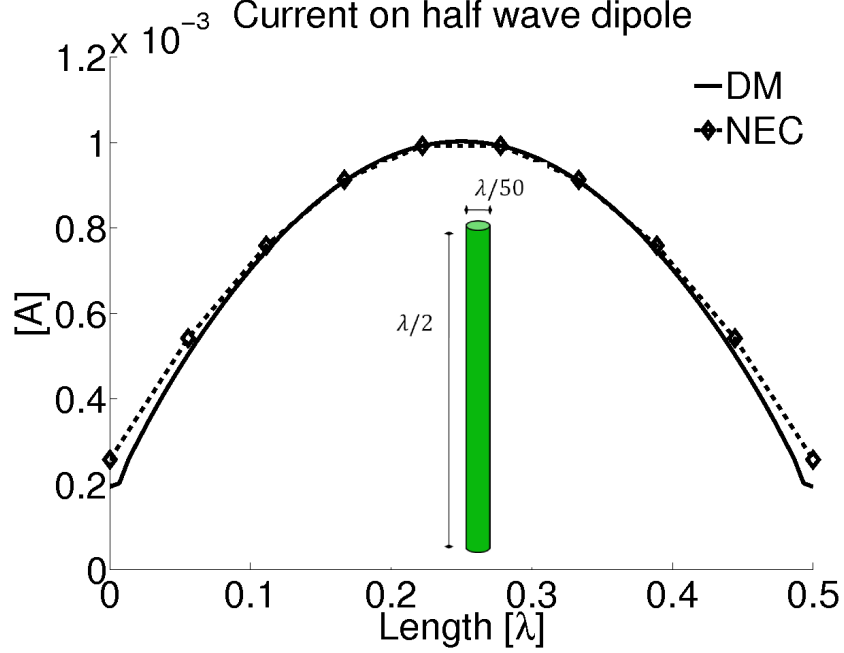


Figure 1.8: Comparison of the magnitude of current distribution on a half-wave dipole of radius $\lambda/100$ and length $\lambda/2$.

1.4 Conclusions

The DM approach utilizes the fact that an induced dipole moment on an electrically small sphere is intrinsically related to the excitation field. We have employed the Dipole Moment approach, in conjunction with the MoM paradigm, to model PEC scatterers by fictitious spheres representing the geometry of the structure being analyzed. The radii of the spheres match those of the wire being modeled. We underscored the advantages of using the DM based formulation for computing the induced currents on PEC structures in the context of the singularity issues associated with the conventional MoM formulation. We have demonstrated the validity of the DM-based formulation, by considering simple PEC wire structures illuminated by arbitrary plane waves. Thus this formulation provides a simple, accurate and numerically efficient method for solving scattering problems of arbitrary shape which may have small features.

We note, however, that since the spacing between the adjacent dipole moments is determined by the wire radius, that if the wire is thin or if the structure is relatively large, we need to define a large number of these moments to handle such problems. This makes the method numerically inefficient for such situations. For example, we need approximately 75 dipole moments for the example of the half-wave dipole (Fig.1.8) as compared to 10 segments for an MoM solver. In fact, the DM approach, per se, is not very efficient due to the large matrix size it generates when the structure size is comparable to λ . To mitigate this problem, in the next chapter we introduce the so-called “characteristic basis function method”, which helps to reduce matrix size significantly as compared to that needed in the DM approach.

2. Macro Basis Functions

2.1 Introduction

In Chapter 1, we introduced an approach to model the induced currents on a small PEC structure in terms of the dipole moments of constituent spheres (Fig.1.3). Numerically, the Dipole Moment (DM) method is analogous to MoM, in that we construct a set of N simultaneous linear equations in the N unknown weights w_n by applying the boundary condition (1.3) at N points along the surface of the structure. In DM, each sphere acts as an individual scatterer, whose dipole moment is related to the total field incident upon it, as seen in (1.10). An attractive feature of the DM approach is that it generates a well-conditioned matrix and offers a self-consistent method for handling the singularity problem associated with the self term of the electric field integral equation (EFIE) based on Green's function. However, the radius of the spheres required to discretize the geometry is determined by the wire radius, which may be very small. Similarly, as we saw in Sec.1.3, if the size of the structure is comparable to the wavelength λ , the number of dipole moments required to model the object is considerably higher than needed in conventional MoM. In order to reduce the number of unknowns and thus contain the size of the matrix generated in the DM method, we introduce in Sec.2.2 a set of functions called the Macro Basis Functions.

2.2 Macro Basis Functions

Macro Basis Functions (MBFs) are simply higher-level basis functions obtained by combining together a contiguous subset of adjacent dipole moments. This is illustrated in Fig.2.1. The envelope of the macro basis functions sets the relative weights of the dipole

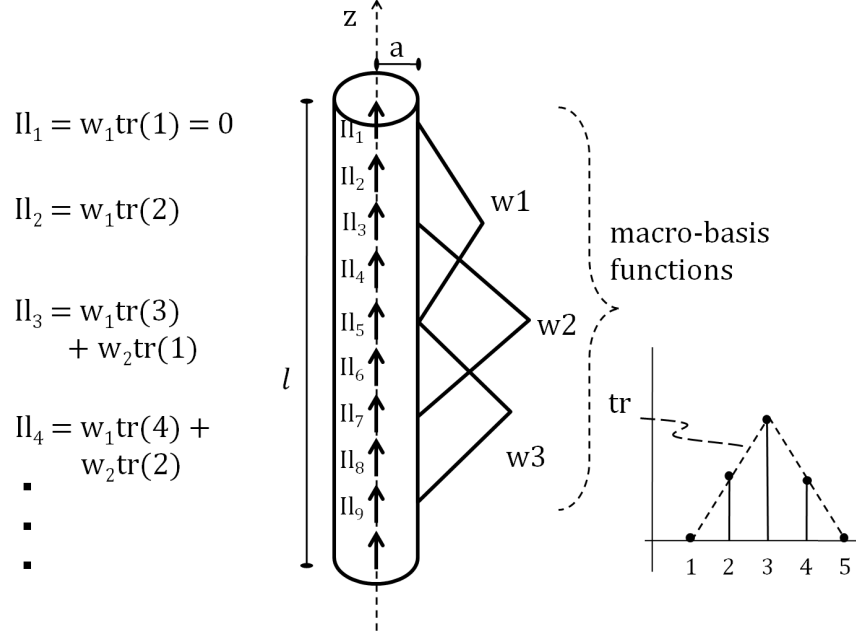


Figure 2.1: **Triangle** MBF employed to combine together adjacent dipole moments. The envelope of the MBF is given by triangle function tr . Figure shows that 9 dipole moments can be weighted and combined by using 3 MBFs which have unknown weights w_i , thereby reducing the number of unknowns.

moments that it combines. The macro basis functions are chosen such that they can accurately map the unknown current distribution on the object being analyzed. In this regard, they are similar to the sub-domain expansion functions used in the conventional MoM. Typical choice for sub-domain macro basis functions are triangles, pulses and RWGs[16]. In Fig.2.2, we demonstrate the use of **triangle** macro basis functions together with the DM method for the simple cases of a PEC wire of length $\lambda/2$ and 1λ . From this figure, we note that the characteristic distribution of current on simple PEC wire structures is

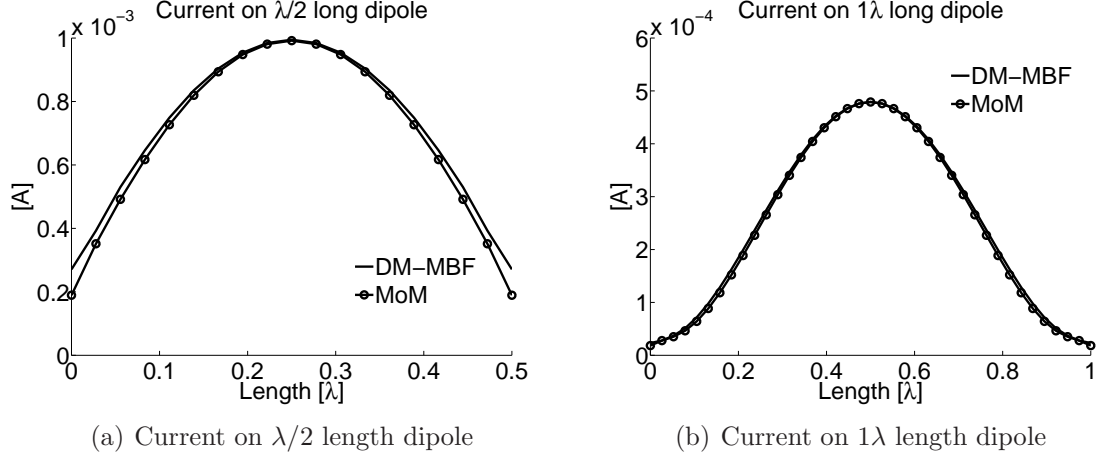


Figure 2.2: Comparison of the magnitude of current distribution on PEC wire (a) $\lambda/2$ dipole (10 unknowns) and, (b) 1λ dipole (20 unknowns).

typically sinusoidal. However, macro basis functions are not restricted to be sub-domain basis functions. In fact, in Sec.2.3, we introduce a set of complete domain macro basis functions for subsequent use in the numerical analysis of doubly periodic arrays and Frequency Selective Surfaces. In summary, macro basis functions provide a way to leverage the computational simplicity of the dipole moment method while maintaining a small matrix size. Hence, the use of macro basis functions allows us to use the dipole moment method to handle electrically large structures by using a matrix size which is comparable to that utilized in formulations based on the MoM.

2.3 Characteristic Basis Functions

Characteristic Basis Functions (CBF) are a set of high-level, entire domain macro basis functions, using which we can reduce the typical matrix size by orders of magnitude as compared to that needed in the conventional DM formulation. We have found that, frequently, as few as one or two CBFs are adequate for representing the induced current. This feature is particularly attractive when analyzing electrically large structures and pe-

riodic arrays. These functions are referred to as the Characteristic Basis Functions (CBFs) because they are tailored to the geometry under consideration and are physics-based[17]. Another feature of the CBFs is that they are linearly independent by construction, hence their use leads us to generate well-conditioned interaction matrices. In Chapter 3, we will demonstrate the versatility of the use of CBFs in solving doubly infinite periodic arrays. We now proceed to develop a method to generate the CBFs which have the above-mentioned attributes.

2.4 Procedure for generating Characteristic Basis Functions

The first step in generating the Characteristic Basis Functions for a given object is to construct the interaction matrix $[Z_{DM}]$ for that object by using either the DM method or a combination of DM and an appropriate set of sub-domain macro basis functions, as for instance triangles. We then illuminate the object with a set of plane waves $\mathbf{E}^{inc} = \mathbf{E}_0 e^{-j\mathbf{k}\cdot\mathbf{r}}$ spanning the $[\theta, \phi]$ space. This is shown in Fig.2.3. We point out that for completeness, we use two orthogonal polarizations for the incident plane waves.

Let $[V^{PWS}]$ be the set of the excitation vectors on the object corresponding to each such plane wave. We then solve for the induced currents $[I^{PWS}]$ for each excitation, by inverting the $[Z_{DM}]$ matrix and express the solution as,

$$[I^{PWS}]_{N \times M} = [Z_{DM}]_{N \times N}^{-1} \times [V^{PWS}]_{N \times M}, \quad (2.1a)$$

where M is the number of plane waves used. Typically, in our numerical simulations for wire structures like the dipole, tripole, loop and split loop, we have found that $M \sim 20$

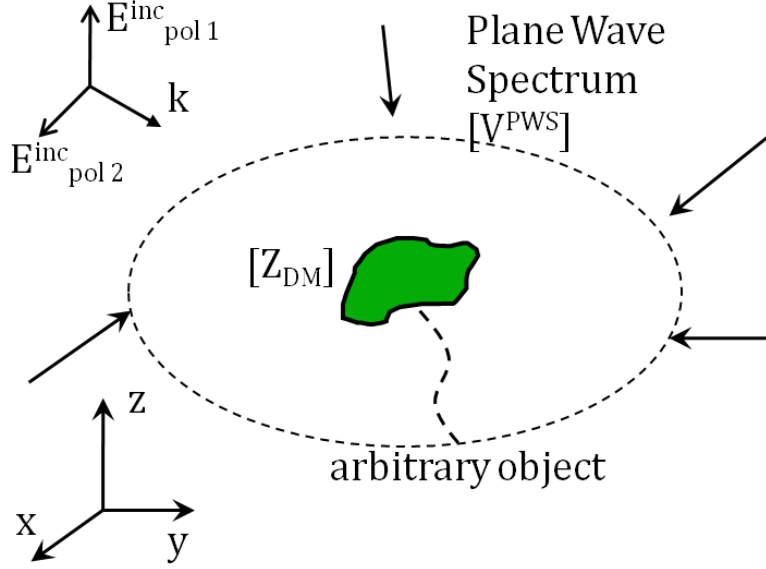


Figure 2.3: Illustration of the use of Plane Wave Spectrum to illuminate a given object. Two mutually orthogonal polarizations are used for each of the incident plane waves.

is sufficient. Next, to form an orthogonal basis set in order to ensure a well-conditioned matrix, we perform a Singular Value Decomposition (SVD) on $[I^{PWS}]$, as follows:

$$[I^{PWS}] = U\Sigma V^T, \quad (2.1b)$$

where \mathbf{U} and \mathbf{V} are unitary matrices and Σ is a diagonal matrix. We now retain only the dominant singular values of Σ by applying a threshold of $\sim 1e-2$ as: $\Sigma_{threshold}(i, i) = 0$ if $\frac{\Sigma(i, i)}{\Sigma(1, 1)} < 1e-2$. The SVD threshold decides the number of CBFs and the accuracy of modeling. The final step is to form the CBFs by using the vector product

$$[I^{CBF}]_{N \times K} = U\Sigma_{threshold}, \quad (2.1c)$$

where K is the number of dominant CBFs. Once we have generated the CBFs, we reduce the original matrix $[Z_{DM}]$ by weighting the interaction fields from individual dipoles with the weights given by the envelop of I^{CBF} . These fields are further “tested” with the

CBFs. This matrix reduction procedure is identical to the Galerkin procedure used in conventional MoM and is given in (2.1d),

$$[Z_{CBF}]_{K \times K} = [I^{CBF}]_{K \times N}^T [Z_{DM}]_{N \times N} [I^{CBF}]_{N \times K}. \quad (2.1d)$$

For PEC wire structures, we find that K , the number of CBFs, is relatively small, typically $K \leq 10$. We note that the above procedure should be performed at the highest frequency in the frequency band of interest. Also, a set of CBFs can be used over a limited frequency band without having to generate them at each individual frequency. In the context of doubly infinite periodic arrays, we need only derive the CBFs for the isolated element, and not for the entire array, as explained in the next chapter.

2.5 CBFs for some standard PEC wire structures

In this section we generate the dominant CBFs for several wire type of PEC structures by using the procedure described in the previous section. For some structures, the dominant CBFs can be constructed by using piece-wise sinusoids and their higher harmonics, which span the entire structure. Note that each figure in this section shows the dominant singular values, and the real and imaginary parts of dominant CBFs for the particular structure.

We begin with the double loop in the $x - y$ plane which consists of a pair of nested loops. The edge lengths of the outer and inner loops are $\lambda/4$ and $\lambda/5$ respectively. Both loops have a radius of $\lambda/100$, (see inset in Fig.2.4(a)). We note that the real part is $O(1e2)$ times the imaginary part for all CBFs for the double loop. This implies that we may use CBFs that are all real. We also note a non-zero DC value for CB #3 for the inner

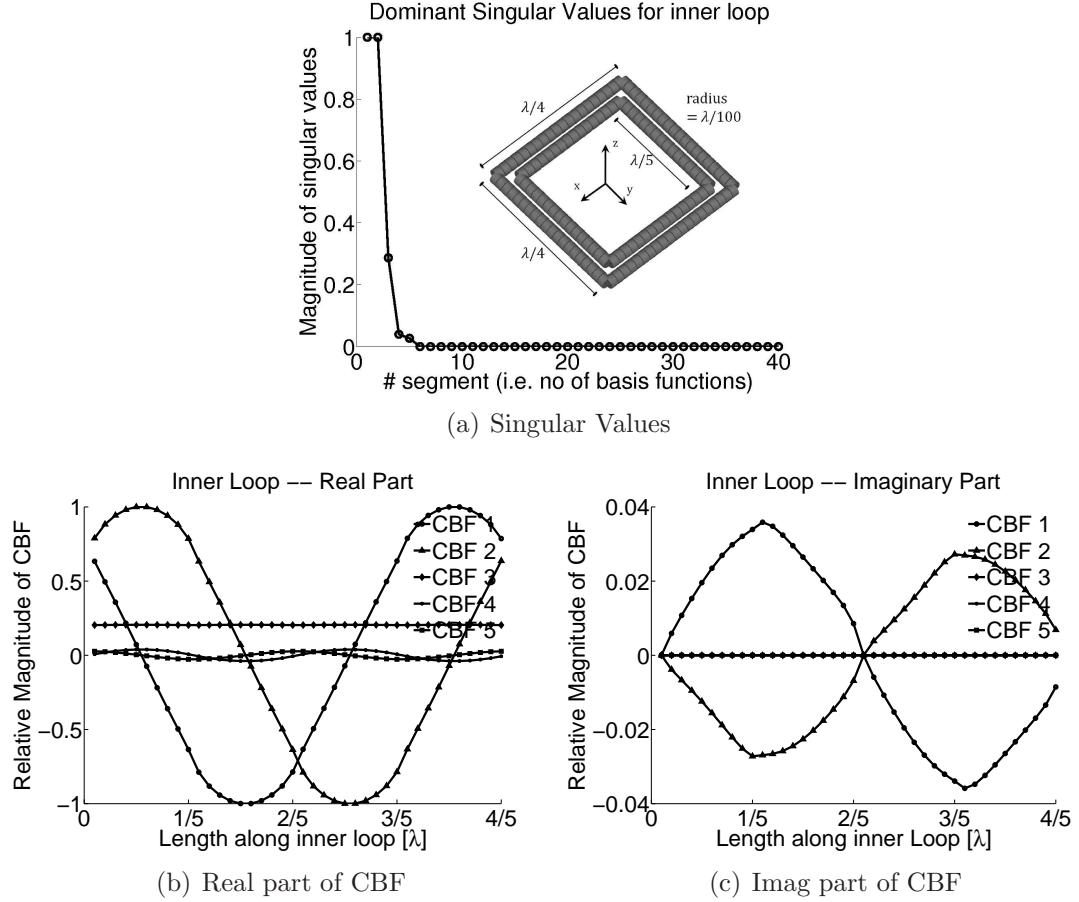


Figure 2.4: (a) Dominant Singular Values, (b) Real Component of CBFs, and (c) Imaginary component of CBFs.

loop (see Fig.2.4(b)), which indicates the mutual coupling via magnetic field between the loops. (The DC component of CBFs for a single loop is insignificant.)

Another geometry of interest is a pair of split loops. This structure is similar to the double loop considered above, except that there is a split along an arm in each loop. Such a structure is commonly referred to as the Split Ring Resonator (SRR) in literature[18]. A doubly periodic structure made of the double split-loop as an element exhibits negative constitutive parameters at certain frequencies, and can be used to synthesize a meta-materials.(citeSRRref) In our example the split is $\lambda/40$, or one-tenth as long as the edge-length of the arm. In this structure, the splits are located on opposite arms of the inner

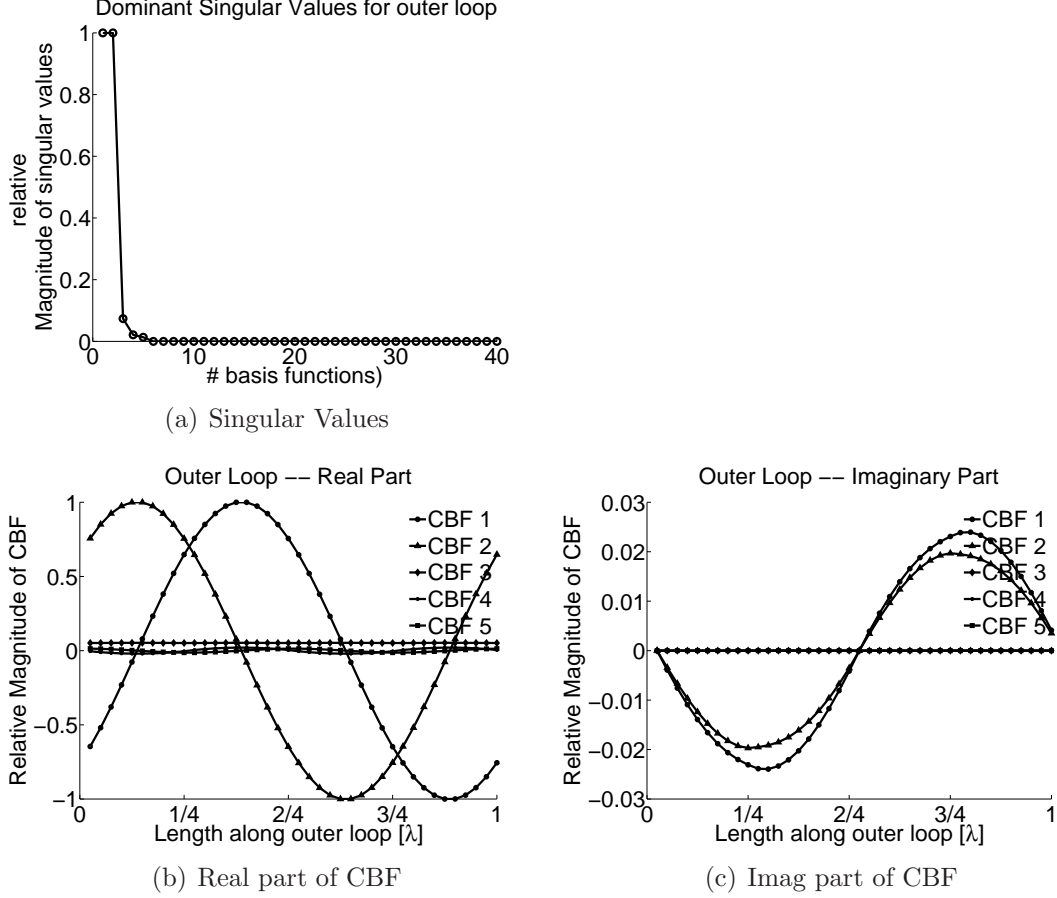


Figure 2.5: (a) Dominant Singular Values, (b) Real Component of CBFs, and (c) Imaginary component of CBFs.

and outer loops, as shown in the inset in Fig.2.6(a). We can clearly see that the current distribution is now influenced by the presence of the split, since it is different from the sinusoidal waveforms that we saw for the double loop in Figs.2.4 and Figs.2.5. Moreover, it is sensitive to the location of the split along the arm, and to the frequency of excitation. This is the reason we need more (six) CBFs to describe the current distribution. We again note that the imaginary component of the CBFs is very small compared to their real counterparts.

In the study of double negative meta-materials, another frequently encountered element is a combination of loop and wire structure of the type shown in the inset in Fig.2.8(a).

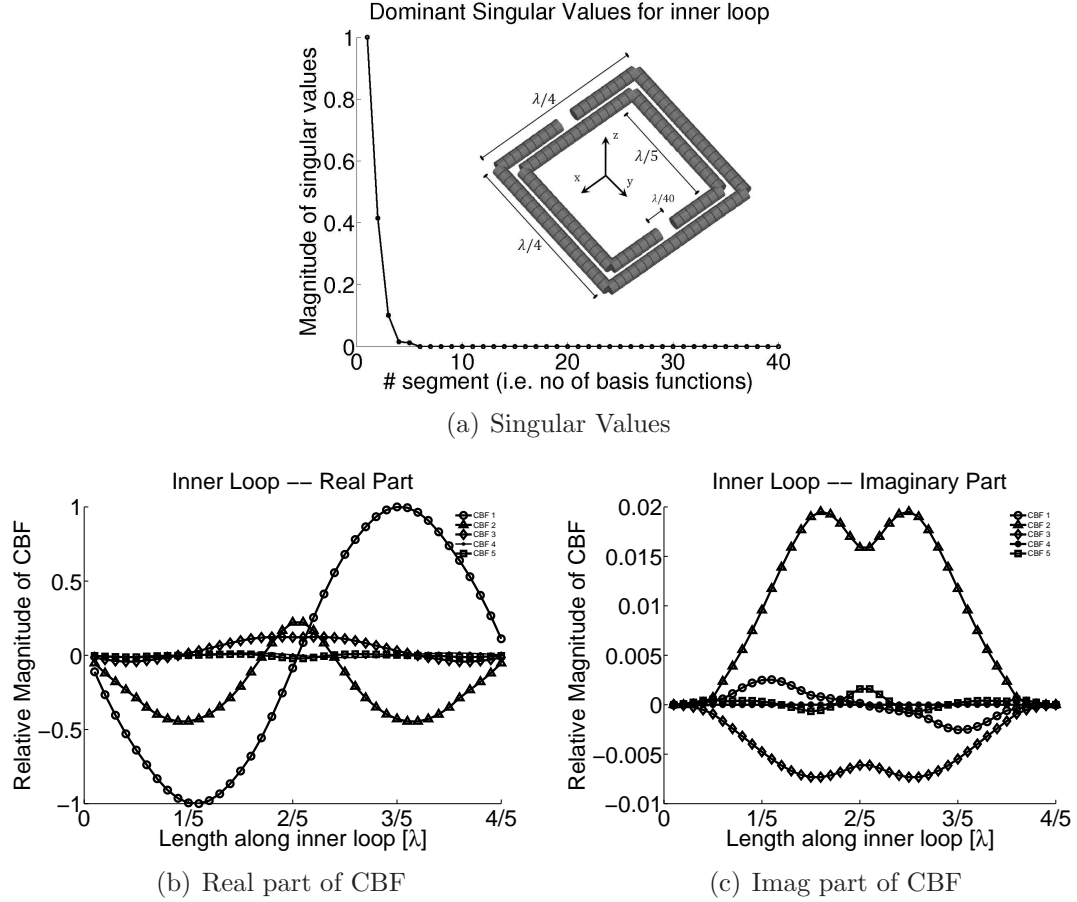


Figure 2.6: (a) Dominant Singular Values, (b) Real Component of CBFs, and (c) Imaginary component of CBFs.

Here, the edge-length of the loop is smaller, ($\sim \lambda/6$; and the length of the wire is $\lambda/4$. The wire is separated from the plane of the loop by a distance of $\lambda/80$. We again note that the dominant CBFs for the loop and the wire are basically real, with their imaginary components being $O(1e-2)$ times the real components. A single CBF is adequate for describing the current on the wire, whereas the loop requires three CBFs. All the CBFs can again be constructed as piece-wise sinusoids.

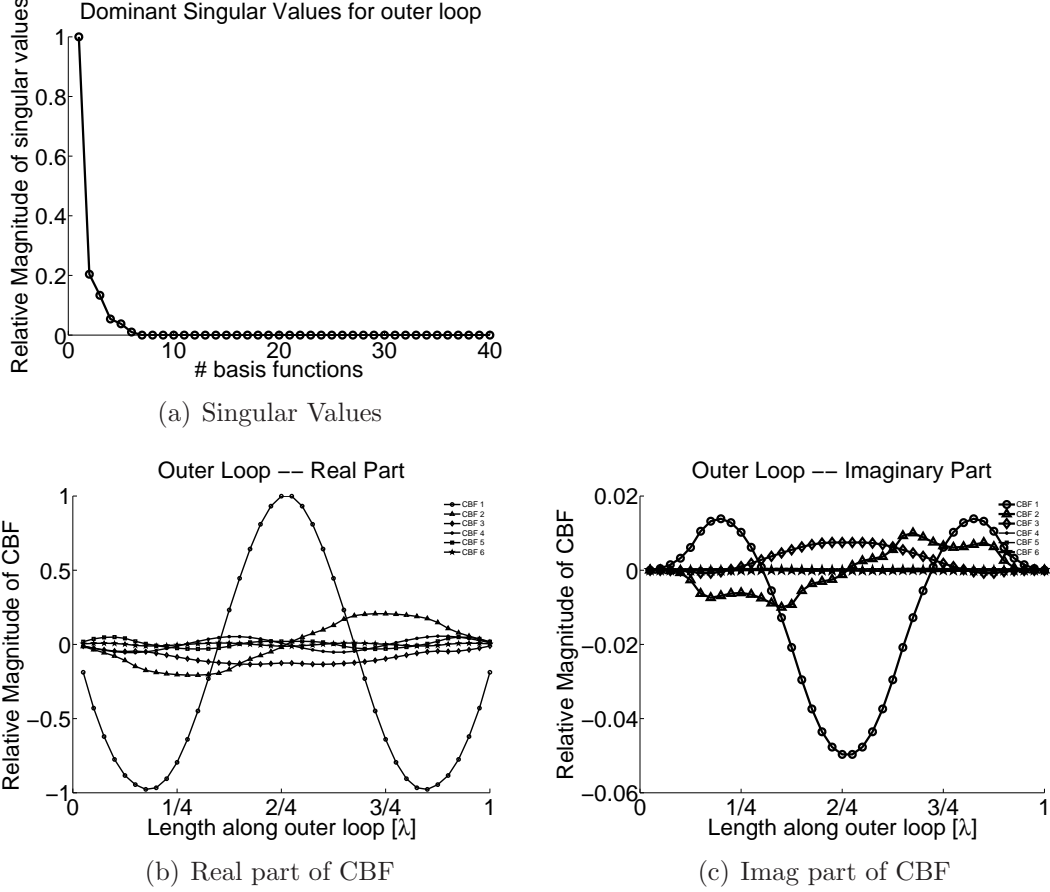


Figure 2.7: (a) Dominant Singular Values, (b) Real Component of CBFs, and (c) Imaginary component of CBFs.

2.6 Conclusion

In this chapter, we have introduced a type of higher-level basis functions called Macro Basis Functions, which help to reduce the size of the Dipole Moment matrix to that comparable to the Method of Moments. In particular, we introduced a special set of entire-domain Macro Basis Functions, called the Characteristic Basis Functions and elaborated upon the method to generate the CBFs for a given object. Since the CBFs are linearly independent by construction, the resultant interaction matrix, $[Z_{CBF}]$, (see (2.1d)) is well-conditioned. We demonstrated that for most typical PEC wire structures, we need very few CBFs to describe the unknown current distribution on them. As long as the frequency

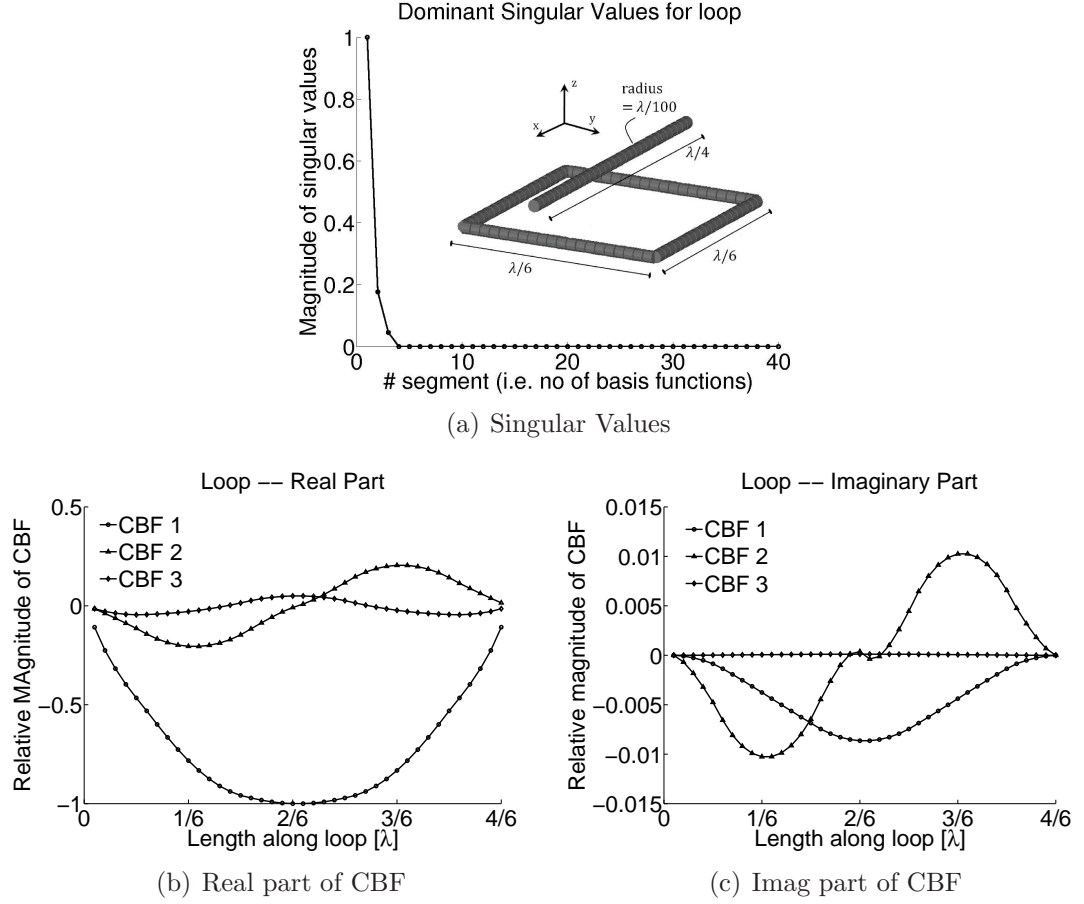
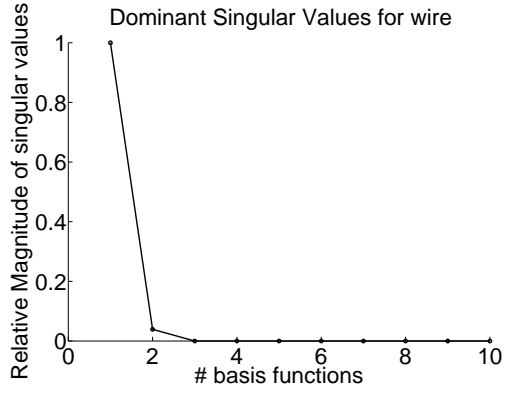
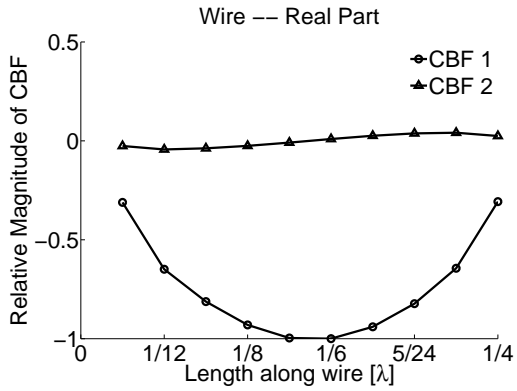


Figure 2.8: (a) Dominant Singular Values, (b) Real Component of CBFs, and (c) Imaginary component of CBFs.

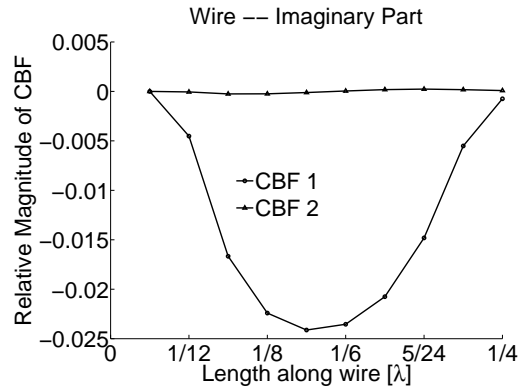
band of interest is reasonably wide, we can use the same CBFs for the object regardless of the frequency of excitation within this band, or of the direction of incidence of the plane wave. In the next chapter, we extend the use of the CBFs to analyze doubly infinite periodic structures.



(a) Singular Values



(b) Real part of CBF



(c) Imag part of CBF

Figure 2.9: (a) Dominant Singular Values, (b) Real Component of CBFs, and (c) Imaginary component of CBFs.

3. Frequency Selective Surfaces

3.1 Introduction

Frequency Selective Surfaces (FSSs) are doubly infinite periodic arrays consisting of metallic or dielectric elements. A typical structure is shown in Fig.3.1. Because of their

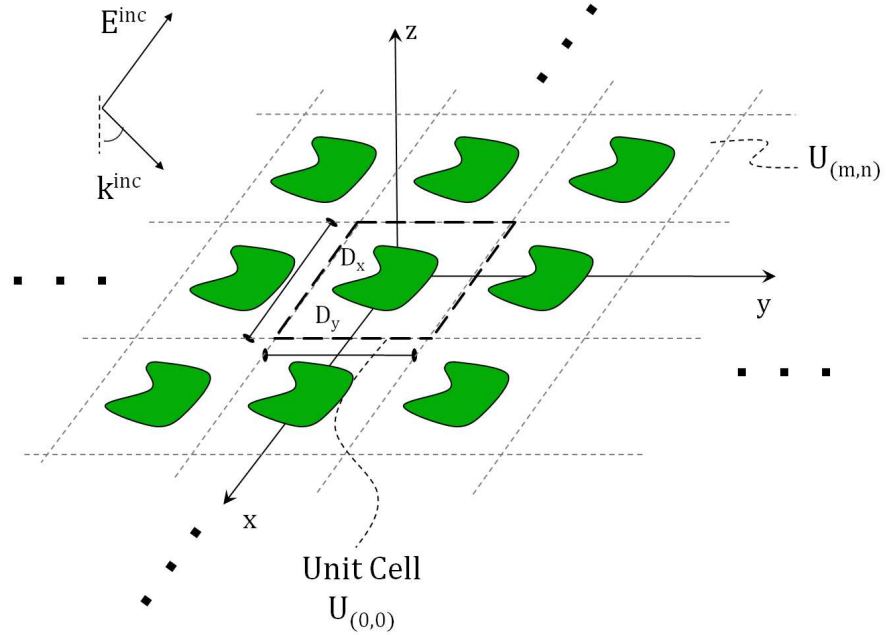


Figure 3.1: Typical geometry of doubly infinite periodic Frequency Selective Surface in the $x-y$ plane. Green area denotes the element. D_x and D_y denote the size of the unit cell.

periodic nature, their reflection and transmission characteristics are sensitive to the fre-

quency of the electromagnetic field incident upon them. Typically, they exhibit a strong reflection in the neighborhood of the element resonance. Their frequency response can be controlled by varying the periodicities along x -, y -, or z -axes. FSS screens are sometimes used as walls of a diffraction grating above and below an electrically small antenna to create a uniform aperture distribution of the near-field and thereby enhance the directivity of the electrically small antenna covered by the FSS[19]. Similarly, they find use as substrates to suppress the surface waves. The frequency sensitive characteristics of FSSs have been leveraged to allow the operation of dual feeds that share the same reflector[20]. Similarly, FSSs have also been used as filters in the microwave spectrum, as well as mirrors to improve the pumping efficiency in molecular lasers[21, 22]. Mittra, et.al. have presented a thorough review of the different techniques that can be used for the analysis of FSSs[23].

At present, a number of Computational Electromagnetic (CEM) tools such as High Frequency Structural Simulator (HFSS), Computer Simulation Technology-Microwave Studio (CST MWS), GEMS (based on the FDTD method) and FEKO (based on the MoM), are available to analyze periodic structures. However, FSS arrays comprising of elements that have multi-scale features are computationally very intensive, and the codes mentioned above may not always be able to solve them in a numerically efficient way. Most codes available for FSS analysis model the elements as strips and they are better suited for analyzing planar elements rather than non-planar geometries. Typically the periodic Green's function is used to generate the interaction fields between the elements of the FSS. However, it is well-known that the expression of periodic Green's function is a very slowly converging series. To accelerate the computation of the terms of the interaction matrix, Ewald transformation[24] may be used to split the infinite periodic sum into its near- and far-field components. The near-field is computed by performing the summation in the spatial domain, while the far-field, which varies slowly, is computed in the Fourier

domain. We note, that the Green's-function-based approach begins by discretizing the strips into surface patches. This requires a large number of unknowns and, hence this approach does not lend itself easily to solving problems involving non-planar geometries. In this chapter, we present a new numerical technique to analyze FSSs, which is based on a combination of the Dipole Moment (DM) Formulation and the Characteristic Basis Functions (CBFs) that were introduced in the earlier chapters. The use of Characteristic Basis Functions ensures that this method would lead to a relatively small matrix. Furthermore, it can solve arrays with unequal periodicity along the x -, y - and z -axes.

To compute the reflection coefficient of the FSS array, we introduce a completely novel and unique technique, based on the concept of reciprocity, which obviates the need to compute the far-fields of the FSS array by integrating the induced current using Green's functions. This technique is very general and is applicable to arrays of arbitrary geometries which may be three-dimensional in nature.

3.2 Formulation

The numerical technique presented in this chapter for analyzing an FSS is based on the premise that a doubly infinite periodic FSS is the asymptotic limit of a corresponding truncated doubly-periodic array. In this section, we describe the technique in detail by considering a simple planar dipole FSS located in the $z = 0$ plane, as shown in Fig.3.2. We use this example not only because it is relatively easy to analyze, but also because a dipole can be used as a constituent block to build more complex elements. Due to its doubly infinite nature, we can identify a unit cell to serve as a geometrical representative of the entire array. The array is thus divided into identical cells, with the unit cell $U_{(0,0)}$ located at the origin. Each cell contains a dipole, which is oriented along \hat{a}_x and which

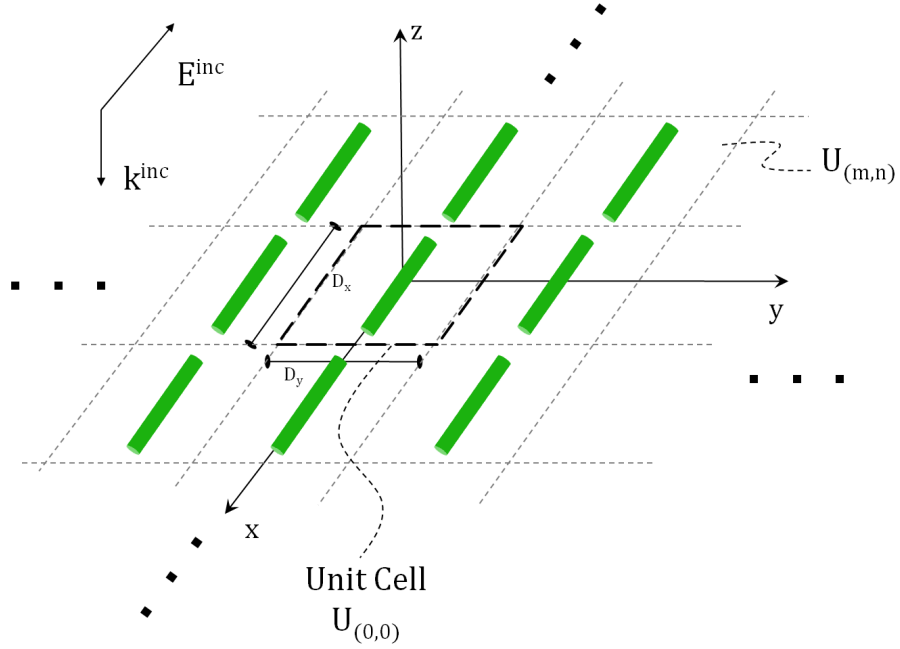


Figure 3.2: FSS screen consisting of thin PEC dipoles. The radius of the dipole is $\lambda/500$ and the size of the unit cell is $0.7\lambda \times 0.7\lambda$, λ is defined at $f = 5 \text{ GHz}$. Plane wave is incident normally, and electric field is polarized along the length of the dipole.

has a radius of $\lambda/500$. The dimensions of the unit cell are $\mathbf{D}_x = 0.7\lambda \hat{a}_x$ along x and $\mathbf{D}_y = 0.7\lambda \hat{a}_y$ along y . For simplicity, we consider a square unit cell conforming to the x – and y –axes of the assumed coordinate system, although any parallelogram where the included angle between \mathbf{D}_x and $\mathbf{D}_y \neq \pi/2$ may be used. We consider an x –polarized plane wave traveling along the $-\hat{a}_z$ direction, which is described by $\mathbf{E}^i = \hat{a}_x E_0 e^{jk_z z}$. Thus the incidence is along a direction normal to the array.

Translation Invariance We begin by first considering a single dipole, and use the DM method to find its CBFs over the frequency range of interest. In this example, the dipole is designed to be resonant at 5 GHz , and the frequency of the incident plane wave varies from 1 GHz to 8 GHz . As can be seen from Fig.3.3(a), only one CBF is required for this element, and it is simply a half-sinusoid over the dipole. Thus its weight w_1 is the unknown that we need to solve. Since every cell of the infinite array is geometrically identical to

the unit cell, we can invoke the principle of translational invariance and assume that the current distribution as well as the EM-fields in any cell are the same as those in the unit cell, apart from a phase shift $\psi(r)$, which is determined by the angle of incidence of the illuminating wave. This is illustrated in Fig.3.2. Thus we can write,

$$f(\mathbf{r}) = \sum_{m,n=-\infty}^{+\infty} f_0(\mathbf{r} - \rho_{mn})e^{\psi(r)} \quad (3.1a)$$

$$\text{where,} \quad (3.1b)$$

$$\psi(r) = -jk_0 \sin(\theta) \cos(\phi)U_m - jk_0 \sin(\theta) \sin(\phi)U_n \quad (3.1c)$$

$$\rho_{mn} = U_m \hat{a}_x + U_n \hat{a}_y$$

where, f_0 represents the field distribution in the unit cell $U_{(0,0)}$; (U_m, U_n) is the location of a general cell; and \mathbf{k}_0 is the wave-vector whose direction is determined by the incident angles (θ, ϕ) . Taking advantage of the translational invariance principle, we can use the same CBF for describing the current over the dipole in any cell $U_{(m,n)}$, as that used for the dipole in $U_{(0,0)}$, but with the appropriate phase shift factor. This fact remains true for an FSS with an arbitrary element geometry and periodicities D_x and D_y that can be different in general. The CBFs, once generated, describe the induced current regardless of the frequency of excitation or the direction of plane wave.

System Matrix As noted earlier, the doubly infinite periodic array is the asymptotic limit of the corresponding truncated array of finite size. We use this fact and the CBFs for the element in $U_{(0,0)}$ to construct the reduced CBF matrix $[Z_{CBF}]$ (by following the procedure elaborated in equations (2.1)) for finite arrays with increasing size. This is shown schematically in Fig.3.3(b), where ‘ring’ denotes a set of dipoles located concentric to $U_{(0,0)}$. The matrix $[Z_{CBF}]$ contains the interaction fields on the dipole in $U_{(0,0)}$ with the dipoles located in all cells, including $U_{(0,0)}$. In this example, we have varied the number of rings from 1 (i.e., array size of 3×3) to 20 (i.e., array size of 41×41). For each truncated

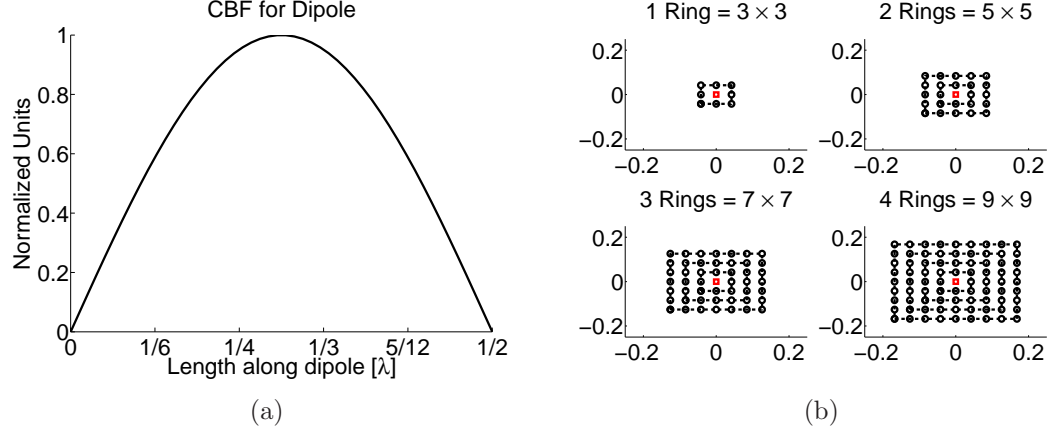


Figure 3.3: (a) Characteristic Basis Function for a single isolated dipole. (b) The size of the finite array, $(2t + 1) \times (2t + 1)$, is increased sequentially by increasing the # of rings t in steps of one. Each circle represents location $U_{(m,n)}$ of the mn^{th} dipole and the central red circle represents the dipole on the unit cell.

array, we solve for the unknown weights of the CBFs, as shown below,

$$[w^{(t)}]_{K \times 1} = [Z_{CBF}^{(t)}]^{-1} [E_{CBF}] \quad t = 1, 2 \dots T, \quad (3.2a)$$

where, $[w] = [w(1), w(2), \dots w(K)]^T$ are the weights of the K CBFs,

$[E_{CBF}]_{K \times 1} = [E_{surf}^{tan}] [I^{CBF}]$ is the tangential component of incident plane wave on the element in $U_{(0,0)}$, which is tested by the same CBFs, and t denotes the total number of rings. The array size in terms of t is simply $(2t + 1) \times (2t + 1)$. At this point we note that the matrix $[Z_{CBF}^{(t)}]$ is stored in the memory each time it is generated. This allows us to update it when the size of the truncated array is increased by adding one more concentric ring of elements, so that only the interaction between the newly added elements and $U_{(0,0)}$ needs to be calculated anew. However, the key point is that the *same* CBFs I^{CBF} are used on each newly added element. Consequently, the size of $[Z_{CBF}^{(t)}]$ remains unchanged no matter how large t (the size of the finite array) becomes. In the present example of the dipole array, the size of this matrix is just 1×1 , since we use only one CBF, even when the finite array has 41×41 dipoles. It is important to note that the weight(s) $w^{(t)}$

do not have any physical significance, per se; this is because, we are not really solving a truncated array problem, since we have assumed that the current distributions in the finite FSS problem are identical to the one in the unit cell apart from a phase shift.

If we observe the behavior of the weight as the array size is increased, it resembles a damped sinusoid as shown in Fig.3.4(a). As seen in Fig.3.4(a), the magnitude of the

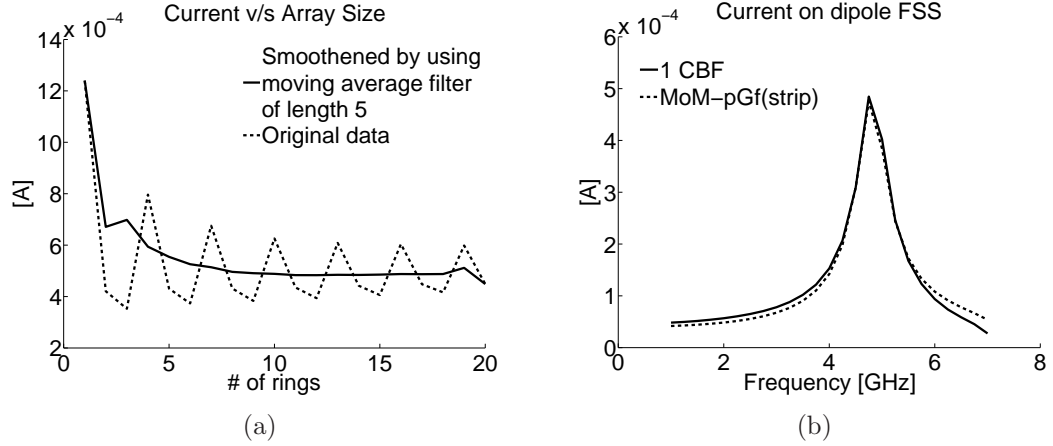


Figure 3.4: (a) Current variation on the dipole in the unit cell v/s size of array (in terms of ‘rings’). The figure also shows the effect of using a moving average filter of length 5. (b) Magnitude of Current on dipole FSS v/s frequency and its comparison with corresponding result obtained by using conventional MoM using periodic Green’s function.

current on the central dipole, which is given by,

$$I = [w]^T [I^{CBF}], \quad (3.2b)$$

exhibits an amplitude behavior that tends to converge, albeit slowly, as the array size increases. To limit the number of simulations of the finite array, we have to define an upper limit on its size parameter T . We do this by using a moving average filter of an appropriate length over the data of Fig.3.4(a). For instance, we used a filter of length 5 to find the mean of five data points, (i.e., $\text{mean}(w^{(t)}, \dots, w^{(t+5)})$). If the mean value varies by $\leq 1\%$ after adding even one more concentric ring of elements, we argue that

the solution for the weight w has converged. We then calculate the final current in the unit cell of the FSS using (3.2b). As can be seen from Fig.3.4(b), the induced current on the dipole FSS computed by using a single CBF agrees well with that derived by using the MoM technique which is based on the use of the periodic Green's function. We also note that the MoM code models the dipole as a rectangular strip whose width was chosen to be equal to the circumference $2\pi r$ of our wire dipole, and requires approximately 30 surface patches to discretize the strip.

3.3 Reflection Coefficient

In the previous section we discussed a numerical technique to solve for the induced current on (the element in the unit cell of) an FSS comprising of PEC structures which can be modeled with wires. In the conventional technique, the first step in computing the reflection coefficient of the FSS array is to find the far-field E_{ff}^{scat} of the induced current. The reflection coefficient is then defined as follows[25]:

$$R \triangleq \frac{E_{ff}^{scat}}{E^{inc}}. \quad (3.3)$$

In this section we introduce a new technique based on the concept of reciprocity to compute the reflection coefficient. We first briefly introduce the reciprocity theorem as it applies to our problem. For a region V bound by a closed surface S which contains two independent sources a and b (both electric and magnetic), we can manipulate the Maxwell's equations to get

$$-\oint_S (\mathbf{E}^a \times \mathbf{H}^b - \mathbf{E}^b \times \mathbf{H}^a) \cdot d\mathbf{s} = \iiint_V (\mathbf{E}^a \cdot \mathbf{J}^b - \mathbf{H}^a \cdot \mathbf{M}^b - \mathbf{E}^b \cdot \mathbf{J}^a + \mathbf{H}^b \cdot \mathbf{M}^a) \cdot d\mathbf{v}. \quad (3.4a)$$

The integral

$$\langle a, b \rangle \triangleq \iiint_V (\mathbf{E}^a \cdot \mathbf{J}^b - \mathbf{H}^a \cdot \mathbf{M}^b) \cdot d\mathbf{v},$$

is referred to as the reaction between the field a and the source b . Since the far-field of a source is a uniform plane wave, we can write $E_\theta = \eta H_\phi$ and $E_\phi = -\eta H_\theta$. If we evaluate the surface integral over a sphere of radius $r \rightarrow \infty$, its left-hand side vanishes. Equation (3.4a) then reduces to:

$$\iiint_V (\mathbf{E}^a \cdot \mathbf{J}^b) d\mathbf{v} = \iiint_V (\mathbf{E}^b \cdot \mathbf{J}^a) d\mathbf{v}, \quad (3.4b)$$

where we have set the magnetic sources \mathbf{M}^a and \mathbf{M}^b to zero. Equation (3.4b) is valid over all space and is known as the ‘reciprocity theorem’. We now consider an interpretation of this equation in the context of our problem. Consider a pair of antennas 1 and 2 as shown in Fig.3.5. The reciprocity theorem then allows us to say[12]: the voltage generated on antenna 2 due to a current source at 1 is identical to the voltage generated on antenna 1 due to the same current source at 2. If we position antenna 2 in the far-field of antenna

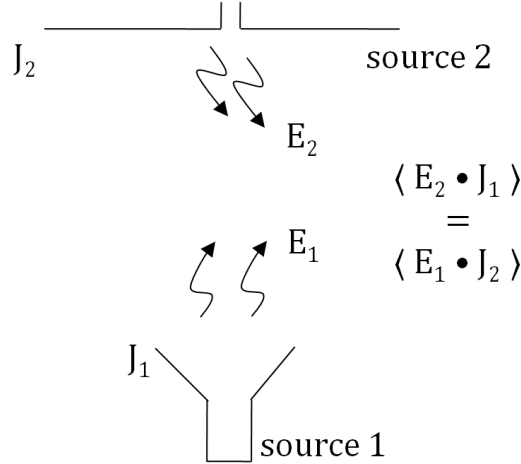
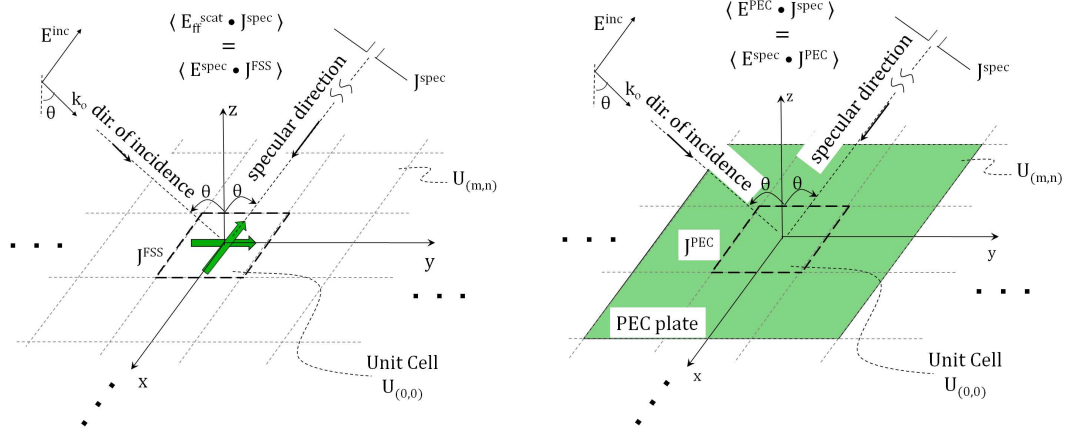


Figure 3.5: Illustration of Reciprocity Principle for a pair of antennas. Magnetic sources are set to zero. $E_{1,2}$ is field radiated by $J_{1,2}$.

1 (ideally at ∞), then the field incident on 1 is very nearly a uniform plane wave, and

according to (3.4b), the reaction $\langle 2, 1 \rangle$ is equal to the reaction of the far-field of the antenna 1 on 2, i.e. $\langle 1, 2 \rangle$. We can therefore state that *the reaction of a uniform plane wave on the current on a given antenna is a measure of the far-field of that antenna along the direction of the plane wave*. Next, we replace the source 1 with the current \mathbf{J}^{FSS} on the FSS array, calculated in Sec.3.2, and replace source 2 with a finite, fictitious source \mathbf{J}^{spec} such that \mathbf{J}^{spec} radiates a plane wave which is incident on the array from the ‘specular’ direction. We note that the ‘specular’ direction denotes the direction of a reflected plane wave given by Snell’s Law. (See Fig.3.6(a)). We denote the reaction $\langle 2, 1 \rangle$ by $\langle \text{SPEC}, \text{FSS} \rangle$,



(a) Problem 1: J_1 is replaced by the current on the FSS: J^{FSS} (b) Problem 2: J_1 is replaced by the current on a doubly infinite PEC plate: J^{PEC}

Figure 3.6: (a) Application of Reciprocity for (a) induced current in FSS and fictitious source J^{SPEC} in far-field, and (b) induced current in PEC plate and same fictitious source J^{SPEC} in far-field. In both figures, specular direction is the direction of the reflected field as given by the Snell’s Law.

such that,

$$\begin{aligned} \langle \text{SPEC}, \text{FSS} \rangle &\triangleq \iint_{U_{(0,0)}} (\mathbf{E}^{spec} \cdot \mathbf{J}^{FSS}) ds \\ &= \iint (\mathbf{E}_{ff}^{scat} \cdot \mathbf{J}^{spec}) ds \dots \text{ using (3.4b),} \end{aligned} \quad (3.5a)$$

where, \mathbf{E}^{spec} is the field radiated by the far-field current source \mathbf{J}^{spec} ; and the former integral is evaluated over the surface of the antenna element in the unit cell. We next

consider a second scenario, where we replace the antenna element of the FSS array with an infinitesimally thin PEC plate, which lies over the entire unit cell. This is just a doubly infinite PEC plate in the x – y plane separating the region $z > 0$ from the region $z < 0$, as shown in Fig.3.6(b). In this second problem, we let the currents on the PEC plate, \mathbf{J}^{PEC} denote the source 1 and we let 2 be the same fictitious source \mathbf{J}^{spec} considered above. We denote the reaction $\langle 2, 1 \rangle$ for this problem by $\langle \text{SPEC}, \text{PEC} \rangle$, so that,

$$\begin{aligned} \langle \text{SPEC}, \text{PEC} \rangle &\triangleq \iint_{U(0,0)} (\mathbf{E}^{spec} \cdot \mathbf{J}^{PEC}) ds \\ &= \iint (\mathbf{E}^{pec} \cdot \mathbf{J}^{spec}) ds \dots \text{ using (3.4b)}, \end{aligned} \quad (3.5b)$$

where \mathbf{E}^{pec} is the field scattered by the doubly infinite PEC plate; and the former integral is evaluated over the unit cell. We note that the source \mathbf{J}^{spec} in both the problems is identical and that it is placed at the same location in the far-field region; hence the incident plane wave, \mathbf{E}^{spec} , emanating from it for each problem is also identical. By defining \mathbf{J}^{spec} along the specular direction, we ensure that it is independent from the source of the actual plane wave which is used as the excitation to calculate the induced currents \mathbf{J}^{FSS} on the array. This implies that the sources \mathbf{J}^{FSS} and \mathbf{J}^{spec} are de-coupled, and hence the conditions for the application of the reciprocity theorem are satisfied. The same argument holds for the sources \mathbf{J}^{PEC} and \mathbf{J}^{spec} . We now proceed to argue that the reflection coefficient defined in (3.3) can be given by an alternative expression involving the definitions in (3.5). We begin by defining the incident, scattered and specular fields as:

$$\mathbf{E}^{inc} = (E_x \hat{a}_x + E_y \hat{a}_y + E_z \hat{a}_z) e^{-j(k_x x + k_y y + k_z z)} \quad (3.6a)$$

$$\mathbf{E}_{ff}^{scat} = R \mathbf{E}^{inc} \quad (3.6b)$$

$$\mathbf{E}^{spec} = (E_x \hat{a}_x + E_y \hat{a}_y - E_z \hat{a}_z) e^{-j(-k_x x - k_y y + k_z z)}, \quad (3.6c)$$

where (k_x, k_y, k_z) are associated with the wave-vector \mathbf{k}_0 , while (E_x, E_y, E_z) are components of incident the electric field \mathbf{E}_0 . Next, we extend the definition of reflection coefficient, as given in (3.3), such that it is equal to the ratio of the reaction of the scattered field, E_{ff}^{scat} on the fictitious source \mathbf{J}^{spec} , and that of the incident field E^{inc} on the same source. Thus, we write

$$\begin{aligned}
R &= \frac{\mathbf{E}_{ff}^{scat}}{\mathbf{E}^{inc}} \\
&= \frac{\mathbf{E}_{ff}^{scat} \cdot \mathbf{J}^{spec}}{\mathbf{E}^{inc} \cdot \mathbf{J}^{spec}} \\
&= \frac{\iint (\mathbf{E}_{ff}^{scat} \cdot \mathbf{J}^{spec}) ds}{\iint (\mathbf{E}^{inc} \cdot \mathbf{J}^{spec}) ds}.
\end{aligned} \tag{3.7}$$

Now, using reciprocity, or (3.5a), we can re-write (3.7) as

$$\begin{aligned}
R &= \frac{\iint_{U_{(0,0)}} (\mathbf{E}^{spec} \cdot \mathbf{J}^{FSS}) ds}{\iint (\mathbf{E}^{inc} \cdot \mathbf{J}^{spec}) ds} \\
&= \frac{\iint_{U_{(0,0)}} (\mathbf{E}^{spec} \cdot \mathbf{J}^{FSS}) ds}{\iint_{U_{(0,0)}} (\mathbf{E}^{spec} \cdot \mathbf{J}^{PEC}) ds} \times \frac{\iint_{U_{(0,0)}} (\mathbf{E}^{spec} \cdot \mathbf{J}^{PEC}) ds}{\iint (\mathbf{E}^{inc} \cdot \mathbf{J}^{spec}) ds} \\
&= \frac{\langle \text{SPEC}, \text{FSS} \rangle}{\langle \text{SPEC}, \text{PEC} \rangle} \times \frac{\iint_{U_{(0,0)}} (\mathbf{E}^{spec} \cdot \mathbf{J}^{PEC}) ds}{\iint (\mathbf{E}^{inc} \cdot \mathbf{J}^{spec}) ds}.
\end{aligned} \tag{3.8}$$

We identify the former multiplicand in the above product as the ratio of the reaction of the specular field on the FSS element to that on the PEC plate. This step enables us to evaluate the reaction integrals over the unit cell, which has a well-defined area, rather than evaluating them over the surface of a fictitious source in the far-field region. It is because of this step that we do not need to characterize the fictitious source beyond saying that it generates the specular field given in (3.6). In other words, this formulation remains independent of shape, electrical size, or the state of polarization of the fictitious source. In this approach, the current \mathbf{J}^{spec} serves to facilitate the derivation of the alternate expression for R . In the final step, we re-write the latter multiplicand in the above

product as

$$\frac{\iint_{U_{(0,0)}} (\mathbf{E}^{spec} \cdot \mathbf{J}^{PEC}) ds}{\iint (\mathbf{E}^{inc} \cdot \mathbf{J}^{spec}) ds} \stackrel{\text{reciprocity}}{=} \frac{\iint (\mathbf{E}^{pec} \cdot \mathbf{J}^{spec}) ds}{\iint (\mathbf{E}^{inc} \cdot \mathbf{J}^{spec}) ds} = -1 \quad (3.9)$$

We have used reciprocity for the former equality. The latter equality follows directly from the fact that $\mathbf{E}^{pec} = -\mathbf{E}^{inc}$, because the ideal doubly infinite PEC plate completely reflects any field incident on it. This fact is the key to this derivation. Stated differently, the property of a PEC plate to completely reflect the incident field enables us to define a reference field (measured in terms of its reaction) for computing the reflection coefficient in the domain of the FSS itself, rather than in the far-field, as required by (3.3). Next, from (3.7), (3.8) and (3.9), and by using the definitions (3.5), we can write

$$R = \frac{E_{ff}^{scat}}{E^{inc}} = -\frac{\langle \text{SPEC}, \text{FSS} \rangle}{\langle \text{SPEC}, \text{PEC} \rangle} \quad (3.10)$$

where the reflection coefficient of an FSS array can be expressed as the ratio of the reaction of a suitably defined specular field over the FSS element and over an equivalent size PEC plate. The advantage of this expression is that we no longer have to find the far-fields of the FSS array by integrating the induced currents via the Green's function. Instead, we simply need to find the reactions prescribed in (3.10). The numerator $\langle \text{SPEC}, \text{FSS} \rangle$ has been defined in (3.5a). Moreover, the reaction $\langle \text{SPEC}, \text{PEC} \rangle$ can be conveniently expressed in closed form, as shown below.

Simplification of the expression for Reflection Coefficient[26]: From Physical Optics, the current \mathbf{J}^{PEC} induced on the PEC plate, with unit area vector \hat{n} , is given as

$$\begin{aligned} \mathbf{J}^{PEC} &= 2\hat{n} \times \mathbf{H}^{inc}|_{z=0} \\ &= 2\hat{a}_z \times \mathbf{H}^{inc}|_{z=0}, \end{aligned} \quad (3.11a)$$

where \mathbf{J}^{PEC} is distributed uniformly over the unit cell. We note that on the $z = 0$ plane, $\mathbf{E}^{spec}|_{z=0} = \mathbf{E}^{inc}|_{z=0} - 2E_z\hat{a}_z$, and the projection of the specular field on this current i.e., $\mathbf{E}^{spec} \cdot \mathbf{J}^{PEC}$ can be expressed as

$$\begin{aligned} (\mathbf{E}^{spec} \cdot \mathbf{J}^{PEC}) &= \frac{2}{\eta_0 |\mathbf{k}_0|} ((\mathbf{E}^{spec} \cdot \mathbf{k}_0)E_z - (\mathbf{E}^{spec} \cdot \mathbf{E}^{inc})k_z) \\ &= -\frac{2|\mathbf{E}_0|^2}{\eta_0} \left(\frac{k_z}{|\mathbf{k}_0|} \right). \end{aligned} \quad (3.11b)$$

Hence, from the definition given in (3.5b), the reaction of the specular field on the uniformly distributed induced current over the PEC plate is expressible as

$$\begin{aligned} \langle \text{SPEC}, \text{PEC} \rangle &= \iint_{U_{(0,0)}} (\mathbf{E}^{spec} \cdot \mathbf{J}^{PEC}) ds \\ &= -\frac{2|\mathbf{E}_0|^2}{\eta_0} \left(\frac{k_z}{|\mathbf{k}_0|} \right) (D_x D_y), \end{aligned} \quad (3.11c)$$

where we note that the ratio $\frac{k_z}{|\mathbf{k}_0|}$ is a measure of the projected area of the FSS unit cell along the direction of \mathbf{k}_0 , and the projected area of the unit cell $|D_x D_y| \hat{a}_z \cdot \hat{k}_0$ reduces for oblique incidence, as expected. Finally, we can re-write (3.10) as

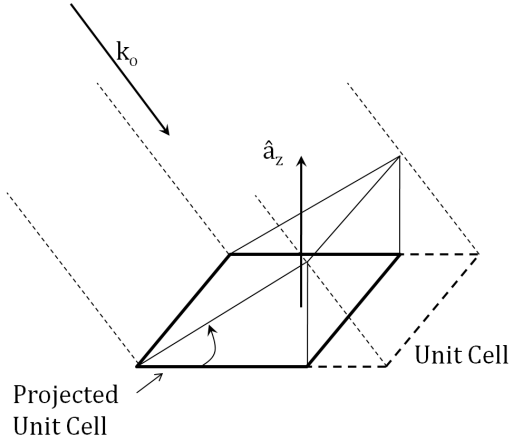


Figure 3.7: Projected area of the unit cell along the direction of incident wave-vector.

$$R = \frac{\eta_0 |\mathbf{k}_0|}{2|\mathbf{E}_0|^2 k_z D_x D_y} \langle \text{SPEC}, \text{FSS} \rangle. \quad (3.11d)$$

To demonstrate the validity of this expression, in Fig.3.8 we compare the reflection coefficient computed by using the currents in fig. 3.4(b) and (3.11d), with those from the MoM-based code. In the next section, we use the method described herein to solve for

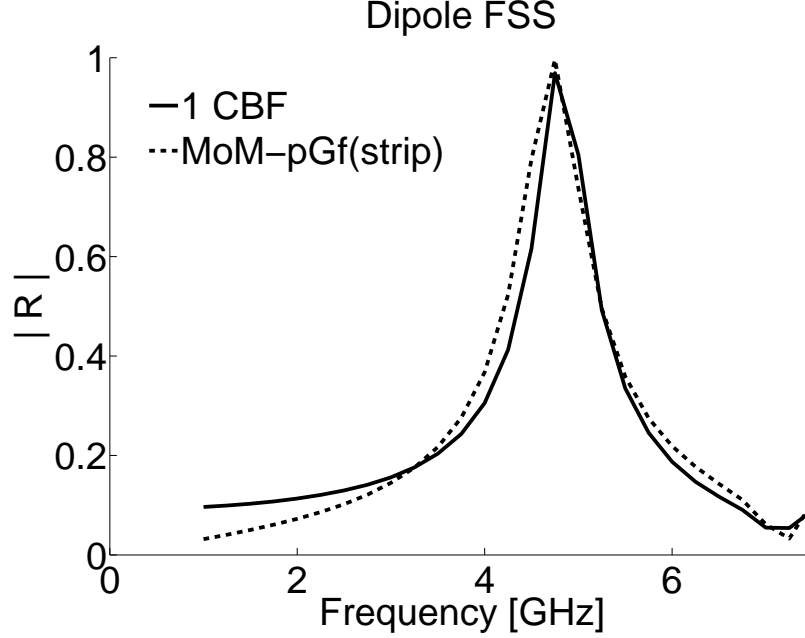


Figure 3.8: Comparison of the magnitude of Reflection Coefficient v/s frequency.

the induced current on the FSS and compute its reflection coefficient for a variety of structures, and we then compare the results with those obtained from existing numerical codes.

3.4 Numerical Results

In this section, we consider three different types of FSS elements: (i) square loop; (ii) split square loop; and (iii) tripole. We have modeled each of these elements as thin PEC wires, although this is not a restriction. This section has been divided into two sub-sections: The

first one, Sec.3.4.1 discusses the results for a planar FSS screen, while Sec.3.4.2 considers a non-planar FSS array. In both the sub-sections we include the results for the case when the illuminating plane wave is obliquely incident on the FSS. To validate our results, we have used two commercially available MoM-based numerical codes: The first code (FEKO), which we refer to as the “MoM code-1”, employs a formulation based on the use of the periodic Green’s function along with the Ewald’s transformation to speed up the convergence of the infinite sum, and the second is a legacy code, which we refer to as the “MoM code-2” [23] in this section. Both codes model the wire elements as thin rectangular strips, and not wires, because of certain limitations in their formulations. For the sake of consistency and simplicity, we have used the following parameters for the structures considered in this section:

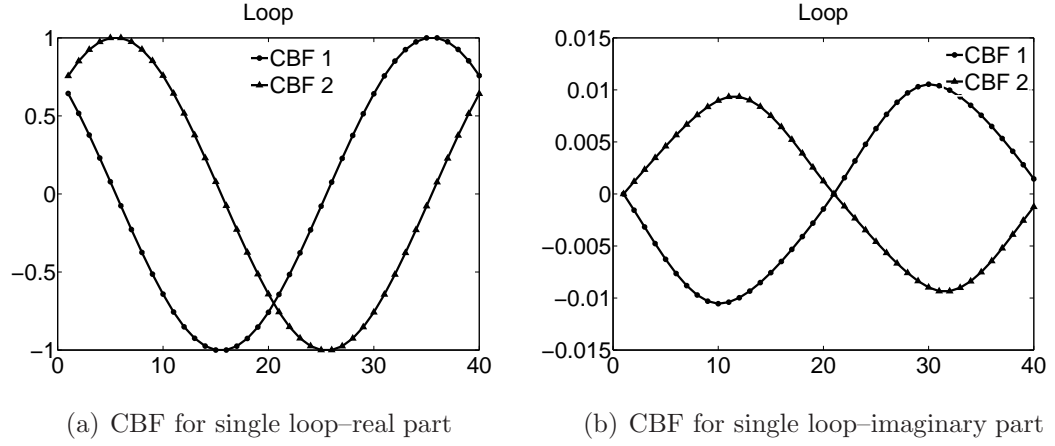
1. Design frequency used for specifying the dimensions of the elements is $f_d = 1\text{ GHz} \Rightarrow \lambda_d = 3e8/f_d [m]$.
2. Radius of wire elements is $a = \lambda_d/500$.
3. Strip width for elements defined in reference numerical codes is $2\pi a$.
4. Frequency of incident plane wave is varied from 900 MHz – 1.4 GHz in steps of 50 MHz .
5. Two cases for the size of the unit cell: (i) $D_x = D_y = 0.5\lambda_d$; and, (ii) $D_x = D_y = 0.7\lambda_d$.
6. Obliquely incident plane wave is always TE_z and its angle of incidence is $\theta \in [0, \pi/6, \pi/4]$.

The results for the reflection coefficient R of the FSS array made of the tripole, presented in this section, are from [27]. Hence, some of the parameters of the geometrical structure and the incident excitation have values specific for those results and may be different from their values given above. As such, they will be pointed out on a case-by-case basis.

3.4.1 Planar Frequency Selective Screens

Square Loop: We have already seen that the currents induced on the FSS element and reflection coefficient for the dipole FSS structure are in good agreement with the corresponding results given by MoM code-1. Next, we consider an FSS screen made of square loops as shown in Fig.3.9(c). The square loop is a symmetrical structure and, hence, finds use as an element in an FSS screen designed to handle two orthogonal polarizations. We note from Fig.3.9(a) and Fig.3.9(b), that only two CBFs are required to model a single isolated square loop; hence the size of the CBF-based matrix for the square loop is 2×2 . We point out that the MoM code-1 requires ~ 100 surface patches, while the MoM code-2 requires 4096 elements to model the loop for the frequency range considered here. Fig.3.10 shows a comparison of R between all the codes for obliquely incident plane waves for a unit cell size of $0.5\lambda_d$. Clearly, all the results compare well with those from the reference codes. Similarly, from Fig.3.11 we note that the numerical results compare well when the cell size is changed to $0.7\lambda_d$ from $0.5\lambda_d$. We note that MoM code-1 is not able to solve the problem beyond a certain higher frequency when the angle of incidence is even slightly off-normal. Also, MoM code-2 suggests a discontinuity at around 0.95 GHz , for the case of $\theta = \pi/6$ and cell size $= 0.7\lambda_d$ (see fig. 3.11(b)). which may not be physical. In contrast to, the Reflection Coefficient curve generated by using the CBF-based method is smooth across the entire frequency range.

Split Loop: Next we consider an FSS screen made of a split square loop as shown in Fig.3.12. The length of the split is $0.1 \times$ the edge-length of the loop, and the split is made along one of the x -directed edges. Fig.2.7 shows that we need six CBFs for the outer loop of a double split loop. Upon applying the procedure discussed in Sec.2.4 to generate CBFs for the single isolated split loop, we again find that six CBFs are sufficient to describe the current distribution over it for the frequency range of interest and their use



Actual Array Geometry [N = 3]

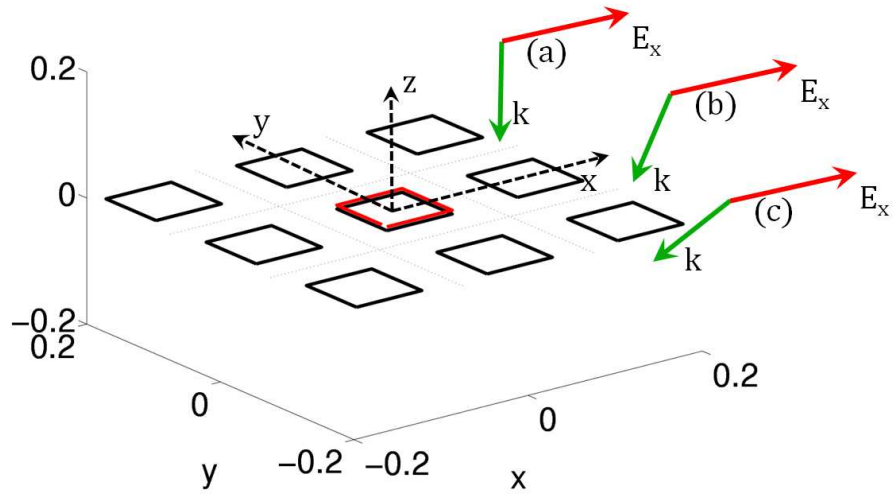


Figure 3.9: Typical geometry of an FSS made of the square loop element in $x - y$ plane. Each edge of loop is $\lambda_d/4$ long. The figure also shows the x -polarized electric field of the incident plane wave for three different cases.

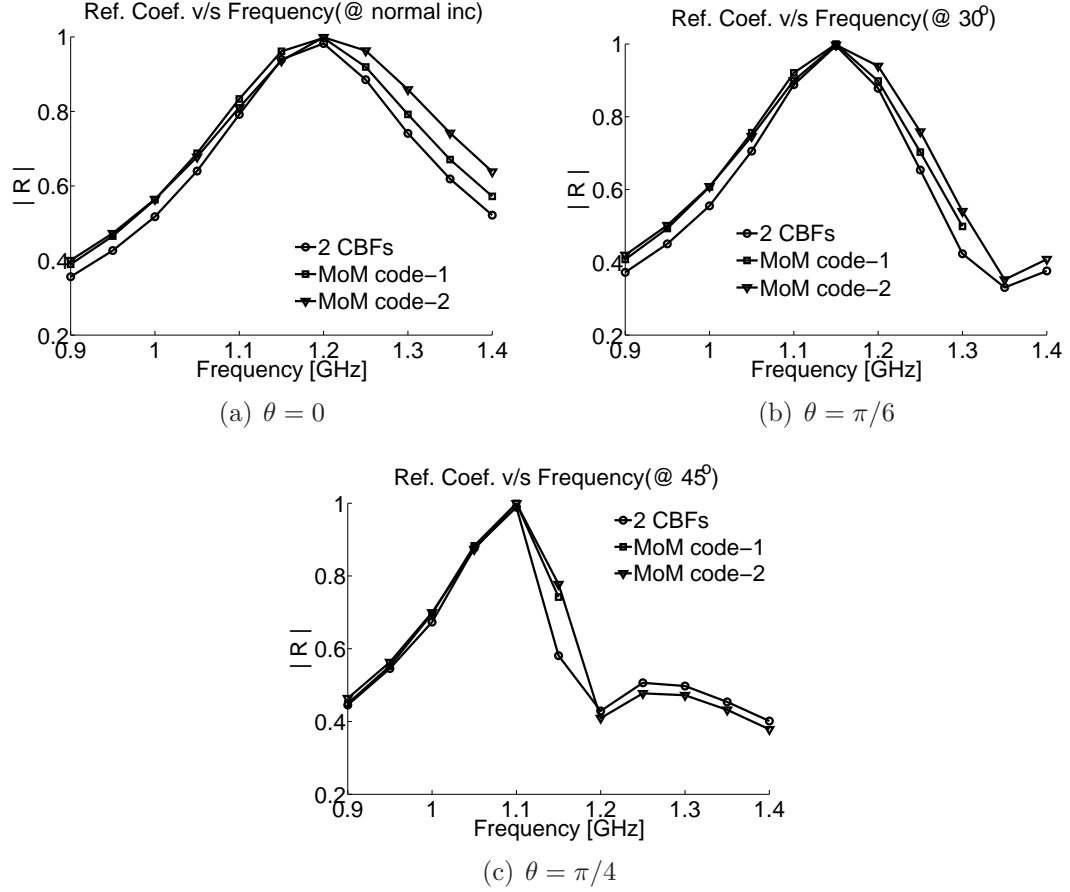


Figure 3.10: Comparison of the magnitude of Reflection Coefficient of FSS of square loop. The cell size is $= 0.5\lambda$. Note that MoM code-1 (curve with square markers) does not generate results for higher frequencies as θ increases.

leads to a matrix size of 6×6 . In contrast, the MoM-based codes, namely code-1 and -2, require ~ 100 surface patches and 4096 elements respectively. Once again we compare R in the same manner as in the case of a square loop. However, here the response is sensitive to the polarization of the incident field because of the presence of the split. Hence, we consider two different cases for this problem. For the first one, the incident TE_z electric field is polarized perpendicular to the split $\Rightarrow \phi^{inc} = 0$ (see Fig.3.13 and 3.14). For this case, the electric field $\mathbf{E}^{inc} = E_y e^{-j\mathbf{k}_0 \cdot \mathbf{r}} \hat{a}_y$, and it cannot ‘see’ the split; in other words, the tangential component of \mathbf{E}^{inc} does not project onto the split. However, we have carefully defined the split in the middle of the x -directed arms, where the current due to the y -polarized incident field goes through a null and changes direction. Hence, the presence

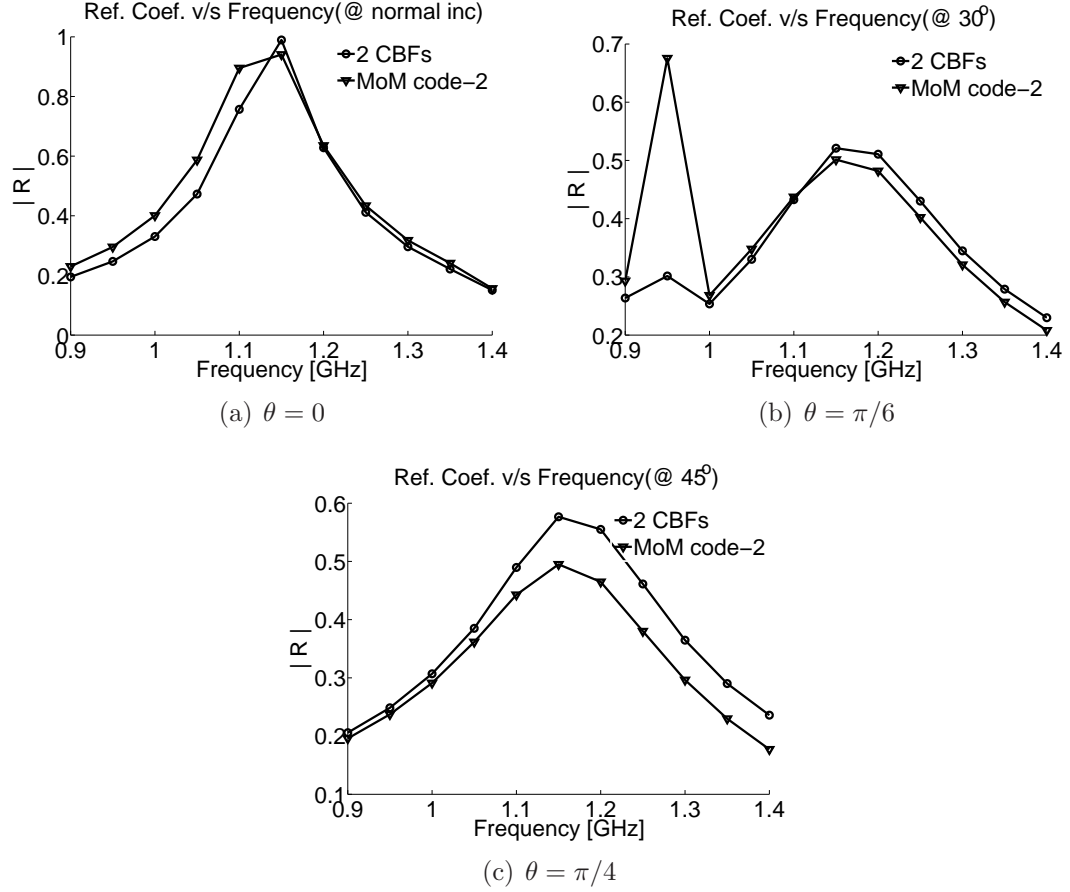


Figure 3.11: Comparison of the magnitude of Reflection Coefficient of FSS of square loop. The cell size is $= 0.7\lambda$.

of the split does not significantly alter the current distribution on the loop, which remains similar to that on a square loop without a split. Consequently, the presence of the split has little effect on the response of the reflection coefficient. If, instead, the split were not located symmetrically on the x -directed arm, the current distribution over the loop would be altered and hence the variation of the reflection coefficient with frequency would differ from that of a corresponding loop without any split. In view of this, we need more than six CBFs to describe the asymmetric current behavior.

For the second case, the incident field is TE_z and its electric field is polarized along the split-bearing arm $\Rightarrow \phi^{inc} = -\pi/2$, and is given by $\mathbf{E}^{inc} = E_x e^{-j\mathbf{k}\cdot\mathbf{r}} \hat{a}_x$. We refer to

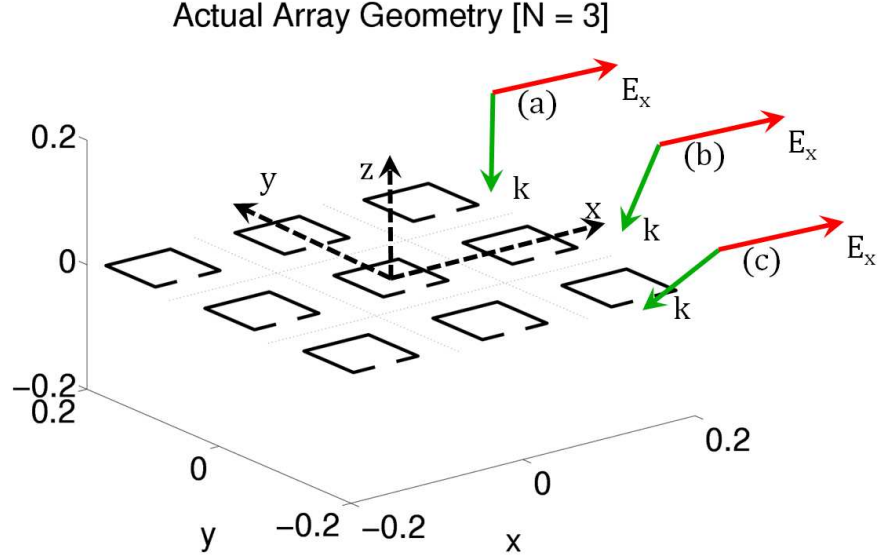


Figure 3.12: Typical geometry of FSS made of split square loop. Each edge of the split loop measures $\lambda_d/4$. The split is of length $\lambda_d/40$ along one of the x -directed arms. The loop itself is in $x - y$ plane. The figure also shows the electric field of the incident plane wave for three different cases polarized along the split-bearing arm.

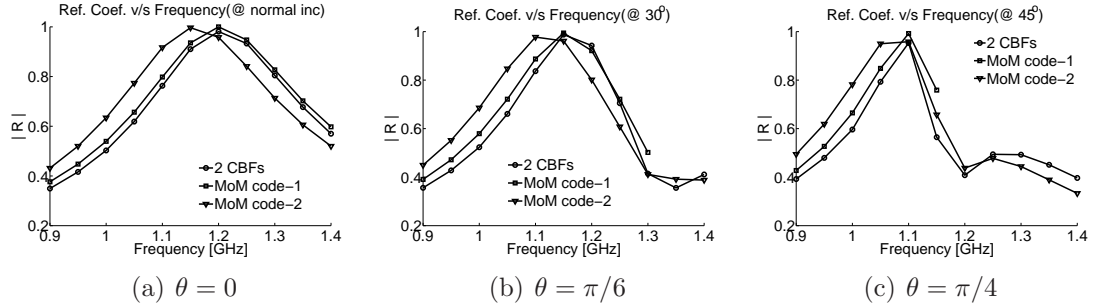


Figure 3.13: Comparison of the magnitude of Reflection Coefficient of a Split Square Loop FSS with unit cell $= 0.5\lambda_d$. The electric field of the incident plane wave used to generate these results is polarized perpendicular to the split-bearing arm. MoM code-1 does not generate results for higher frequencies as θ increases.

Fig.3.15 and 3.16) for this case. Since the incident field has a finite projection along the split-bearing arm, the peak level of the current is lower in this case than in case when the incident field is perpendicular to it. We note from these figures that, for this case, the FSS of split square loop does not exhibit resonant behavior in the considered frequency range. This implies that most of the incident power is transmitted through the FSS screen. This discussion emphasizes the polarization-sensitive nature of an FSS screen whose elements

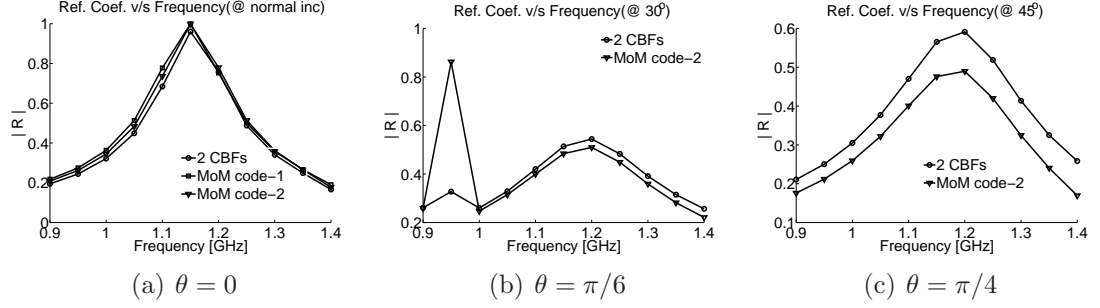


Figure 3.14: Comparison of the magnitude of Reflection Coefficient of a Split Square Loop FSS with unit cell $= 0.7\lambda_d$. The electric field of the incident plane wave used to generate these results is polarized perpendicular to the split-bearing arm. MoM code-1 does not generate results for higher frequencies as θ increases.

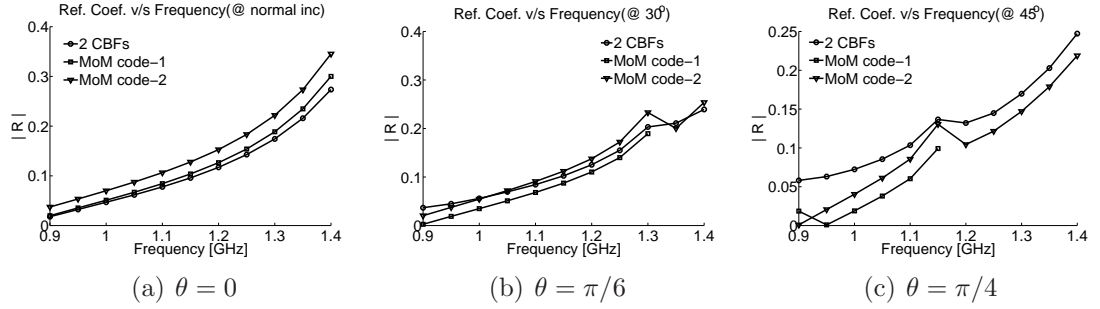


Figure 3.15: Comparison of the magnitude of Reflection Coefficient of a Split Square Loop FSS with unit cell $= 0.5\lambda_d$. The electric field of the incident plane wave used to generate these results is polarized along the split-bearing arm.

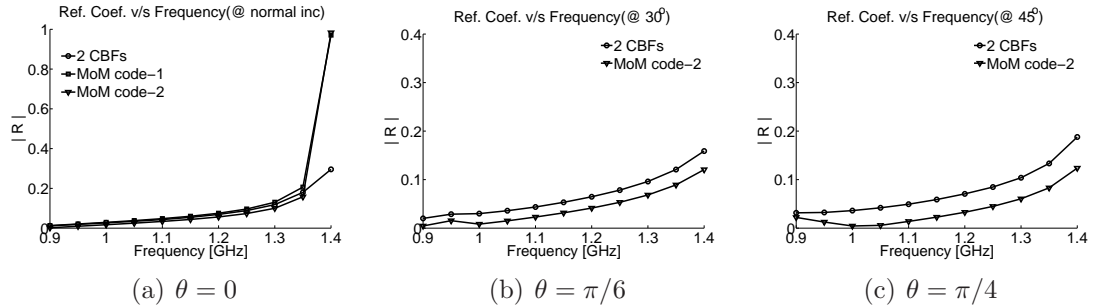
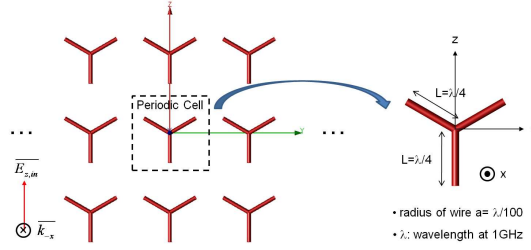


Figure 3.16: Comparison of the magnitude of Reflection Coefficient of a Split Square Loop FSS with unit cell $= 0.7\lambda_d$. The electric field of the incident plane wave used to generate these results is polarized along the split-bearing arm.

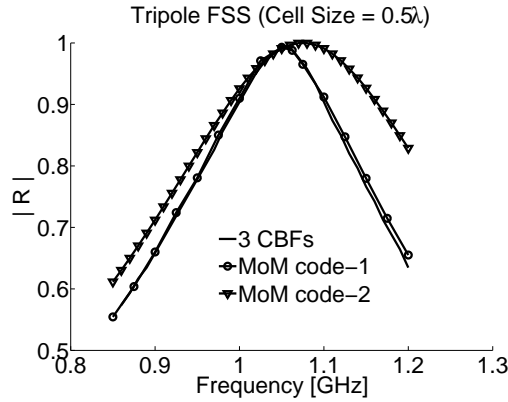
are split square loops. As a final comment, we state that, if the capacitance introduced by the split is increased by using another concentric split loop which lies within this single split loop, as in the case of the well-known split ring resonator (SRR), then the

resonance frequency will shift to a lower value. Such an SRR structure, (shown in the inset in Fig.2.6(a)) finds application in the design of double negative meta-materials, i.e., materials engineered to have negative constitutive parameters.

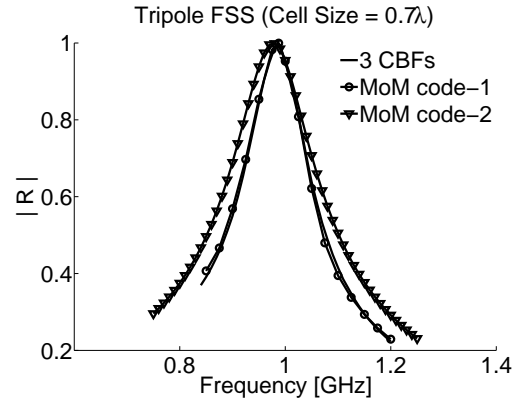
Tripole: The tripole structure consists of three arms, each $\lambda/4$ long, which are oriented such that the included angle between the adjacent arms is 60° . The tripole element considered in this example is designed at a wavelength corresponding to $f = 1\text{GHz}$, and each arm has a radius of $\lambda/100$. (See Fig.3.17(a)). Two cases for the unit cell size are considered: (a) 0.5λ , and (b) 0.7λ . In Fig.3.17 we have presented a comparison of results for the reflection coefficient of an FSS comprising of the tripole element. The source of these results is [27]. We note that three CBFs have been used for the tripole element, one



(a) FSS made by using tripole as an element



(b) Cell Size = 0.5λ



(c) Cell Size = 0.7λ

Figure 3.17: (a) Geometry of tripole element, and the corresponding FSS. The FSS is located in the $y - z$ plane. Electric field is polarized along \hat{a}_z and is incident normally on the FSS. (b) Comparison of R results for FSS with cell size of 0.5λ , and (c) Comparison of R results for FSS with cell size of 0.7λ .

for each arm, to describe the distribution of the induced current. The envelope of each CBF is described by a half-sinusoid function extending over the arms which are quatre-wave long. The related CBF-matrix for the tripole FSS is of size 3×3 , whereas the MoM code-1 uses a matrix size of ~ 100 , and the MoM code-2 uses 4096 unknowns, as for the earlier examples. We note that the results for the reflection coefficient obtained from our technique and that from the commercial MoM codes agree well with each other.

We end this subsection by concluding that the numerical technique described in this chapter is able to handle FSS screens of arbitrary planar geometries and arbitrarily incident plane waves.

3.4.2 Non-planar Frequency Selective Arrays

We begin by noting that the legacy code MoM code-2 cannot handle non-planar FSS arrays. Hence, in this subsection, we will use only the MoM-based code to validate our results. We will demonstrate the versatility of our numerical technique by analyzing a non-planar FSS array having the same split loop used in the previous subsection. Towards this end, we tilt the square loop about the x -axis, as shown in Fig.3.18, to render the geometry non-planar. The unit cell size for this example is $0.5\lambda_d$. It is important to note that we use the same CBFs for the tilted loop as for the planar loop. Hence the size of the CBF matrix remains 2×2 even for the non-planar FSS array. As before, the MoM code-1 uses ~ 100 surface patches to model the tilted loop. We next present the comparison between the reflection coefficient in Fig.3.19. Note that the MoM code-1 models the loop as rectangular thin strips whose width is equal to the circumference $2\pi a$ of the wire modeled in our code. Because of this difference in geometry, the reflection coefficient curve calculated using MoM and the periodic Green's function exhibits a wider

Actual Array Geometry [N = 3]

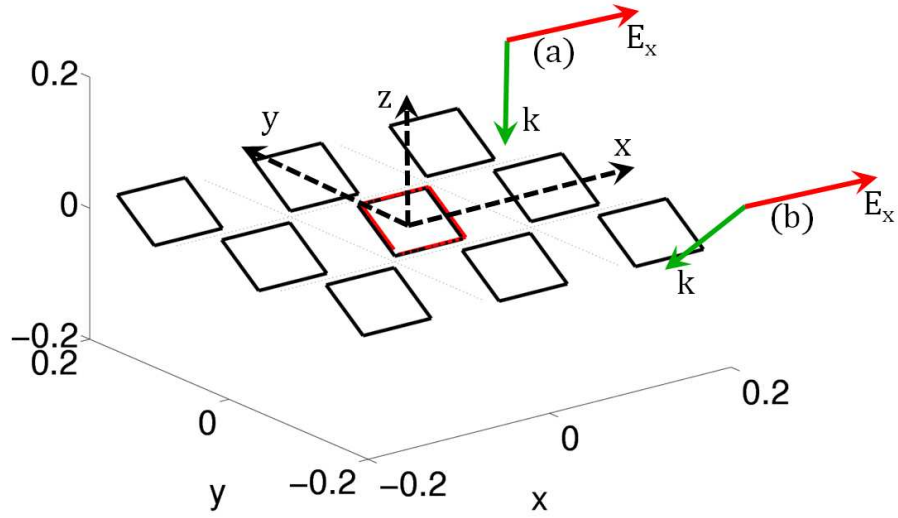


Figure 3.18: Geometry of FSS comprising of square loops that are tilted out-of-plane by an angle $\pi/4$ about the x -axis. The cell size is $0.5\lambda_d$.

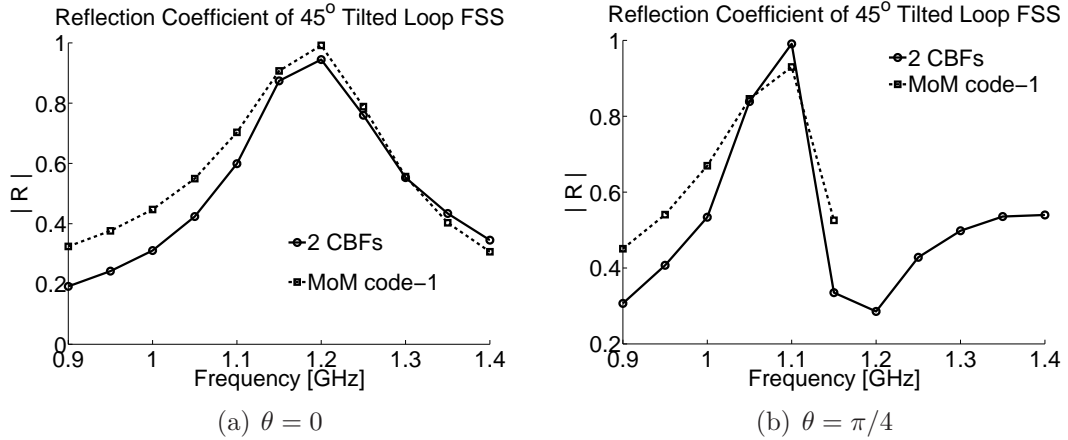


Figure 3.19: Comparison of magnitude of reflection coefficient. (a) Incident plane wave is directed along the \hat{a}_z direction, and (b) Incident plane wave directed at an angle $\theta = \pi/4$ to \hat{a}_z . Electric field is polarized along \hat{a}_x . Note that the bandwidth of the curve for R is narrower in the wire model (our code) than that of the strip model (MoM-based code).

bandwidth than does the result from our code, as shown in Fig.3.19. This is in agreement with the established understanding that thicker antennas have wider bandwidths than their thin-wire antenna counterparts. In fact, we observe this difference in bandwidth depends, to varying degrees, on the element geometry, the cell size, and the direction of

the incident plane wave in all the results presented in this section which compare R from our code with the MoM-based code.

In the next example, we go a step further and tilt the loop by 90° about the x -axis. Thus the FSS array now resembles a stack of square loops parallel to the $x - z$ plane. These loops extend back-to-back along the entire y -axis and edge-on along the entire x -axis, as shown in Fig.3.20. We use the same unit cell size of $0.5\lambda_d$ for this example,

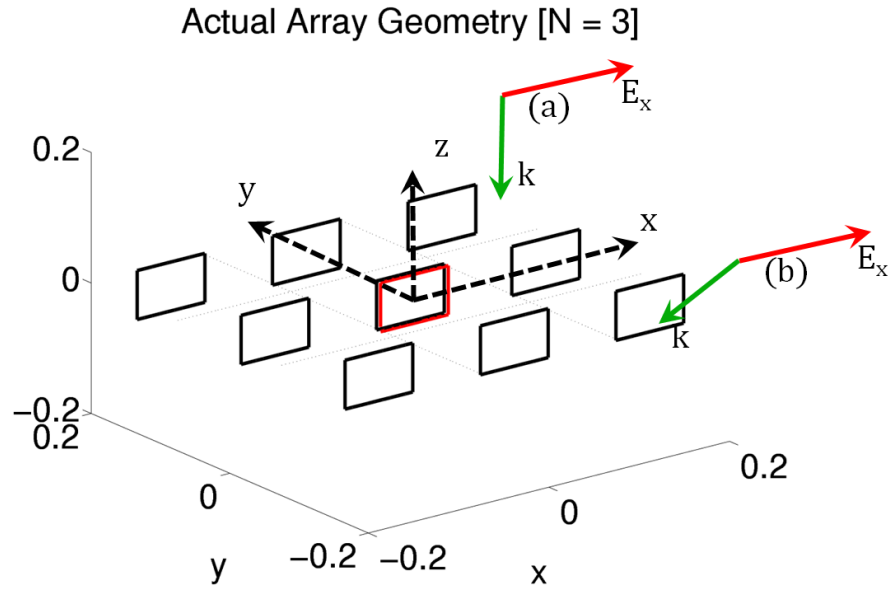


Figure 3.20: Geometry of FSS comprising of square loops that are tilted out-of-plane by an angle $\pi/2$ about the x -axis. The cell size is $0.5\lambda_d$.

and note that once again two CBFs are sufficient to describe the current distribution. This brings out an interesting property of the Characteristic Basis Functions – namely, that once the CBFs for a particular object have generated, they can equally well describe the current on any doubly infinite periodic FSS array made by an arbitrary orientation of that object. This is in addition to their property of being independent of the frequency (over a reasonable frequency band) and the direction of the incident plane wave. Fig.3.21 compares the frequency response of the FSS of Fig.3.20 computed using our code with

that calculated by the MoM code-1. The figure shows that there is a good agreement

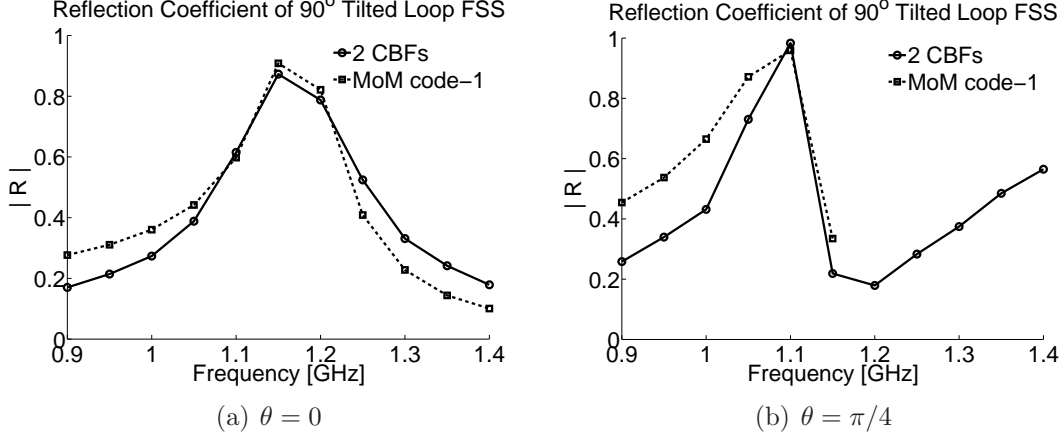


Figure 3.21: Comparison of magnitude of reflection coefficient, (a) Incident plane wave is directed along the \hat{a}_z direction, and (b) Incident plane wave directed at an angle $\theta = \pi/4$ to \hat{a}_z . Electric field is polarized along \hat{a}_x . Note that the bandwidth of the curve for R is narrower in the wire model (our code) than that of the strip model (MoM-based code).

between the two methods for both cases, with the MoM code able to solve only for lower frequencies when $\theta = \pi/4$. This example demonstrates a crucial feature of our numerical technique, namely that it lends itself very easily for the analysis of a multi-layered FSS structure and demands only as much computational time and memory as is required by a conventional, planar and single layer FSS screen.

It is interesting to observe the induced current on the FSS array of the square loop as each element is tilted out-of-plane as described above. (See Fig.3.22). In each of the three cases, the incident field is $\mathbf{E}^{inc} = E_x e^{-jk_z z} \hat{a}_x$. Hence the magnetic field is $\mathbf{H}^{inc} = H_y e^{-jk_z z} \hat{a}_y$ and is polarized along \hat{a}_y . Thus, as the loop tilts, the magnitude of the product $\hat{n} \cdot \hat{a}_y$ increases and with it the flux of the incident magnetic field captured by the projected the area of the loop is higher. Moreover, due to the tilt, the mutual inductance of the loops along the y -axis also increases due to magnetic flux linkage between the loops facing each other. Together, these two effects serve to induce a higher current in the FSS element, as may be seen by referring to Fig.3.22.

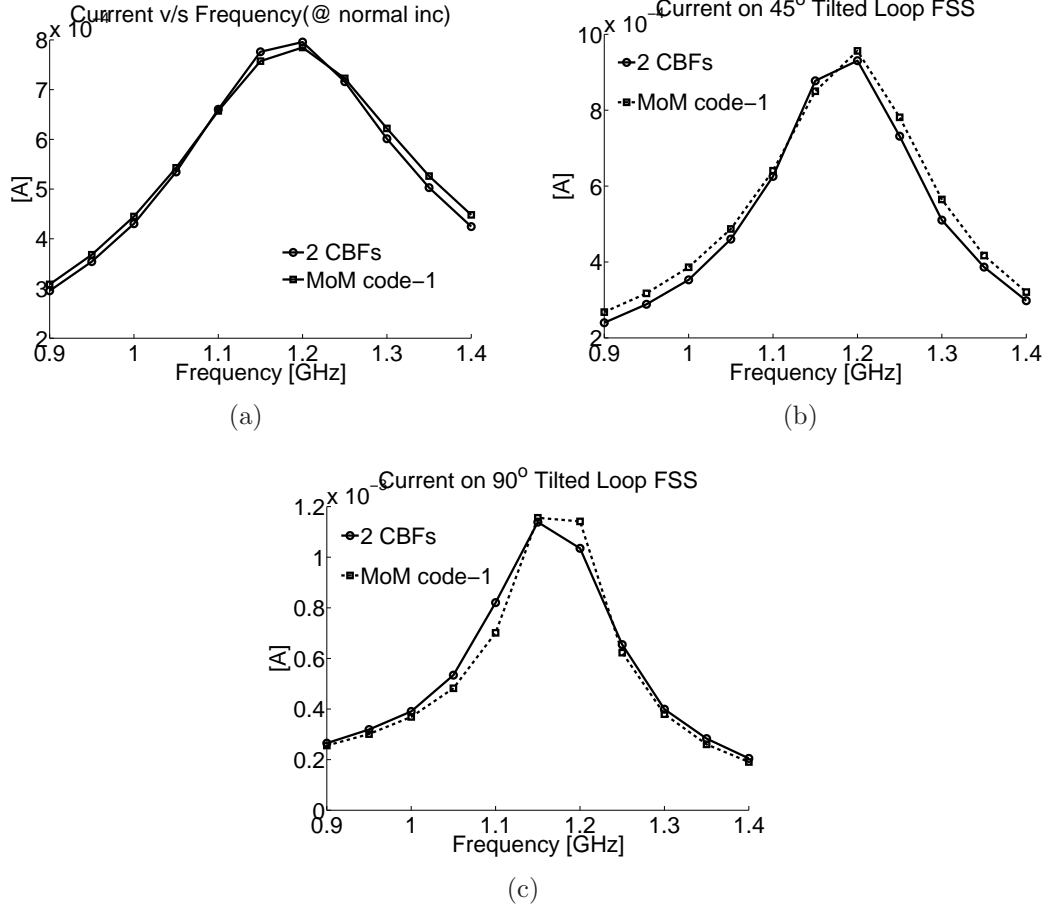


Figure 3.22: Frequency response of the current as the square loop is tilted out-of-plane about the x -axis. (a) 0° tilt [no tilt], (b) 45° tilt (c) 90° tilt. The magnitude of induced current on the square loops is higher with increasing tilt due to enhanced coupling via magnetic field between elements along y -axis, and interaction of incident magnetic field with each loop.

3.5 Conclusion

In this chapter, we have introduced a numerical technique for analyzing a Frequency Selective Surface which begins by generating the Characteristic Basis Functions of a PEC element using the Dipole Moment method. We have invoked the principle of translational invariance and have used the CBFs to construct the interaction matrices for the truncated array of increasing size that are considerably smaller than the conventional MoM matrix. Moreover, the size of the newly-derived matrix does not increase as we increase of size

the finite array. We have shown how we can post-process the solution for the currents on a finite size array, to arrive at the final results for the doubly periodic and infinite FSSs. We have found that the results for the induced currents and the reflection coefficient compare well to those derived from the existing commercial numerical codes. We have pointed out that our approach is capable of handling more general FSS element geometries than we can handle with existing MoM-based codes. Furthermore, we introduced a novel method for finding the reflection coefficient of the FSS array from the induced currents, that obviates the need to integrate the induced currents by using the periodic Green's function. We have presented a number of examples to show that our technique can be used to analyze planar, non-planar, and even multi-layered FSS arrays of (electrically thin) PEC structures of arbitrary shape and that the angle of incidence can be arbitrary as well. In contrast, we have found that an MoM-based commercial code that we have used, i.e., MoM code-1, cannot handle higher frequencies for obliquely incident excitation, while the legacy code MoM code-2, is unable to analyze non-planar FSS arrays.

4. Conclusions and Future Work

Frequency Selective Surfaces are doubly infinite periodic surfaces which exhibit a frequency-sensitive behavior that can be tuned to match the desired transmission characteristics of the application of interest. To mention some of their applications, FSSs may be used as a superstrate to enhance the directivity of electrically small antennas, or, as a frequency selective screen to allow the operation of dual feeds that share the same reflector, in a frequency reuse scheme. An FSS array made of suitably designed elements can exhibit negative constitutive parameters over the frequency range of interest. Such materials, called meta-materials, currently form a very active area of research. In this thesis we have introduced a new numerical technique and explored its use for the analysis of planar and non-planar FSSs comprising of arbitrary PEC elements.

Chapter 1 discussed a computationally simple approach, the Dipole Moment method, which avoids the direct use of the Green's function to find the induced currents on the surface of a PEC object. In the DM method, we used a string of spheres to model the unknown current distribution in terms of the dipole moments induced in each sphere due to a given illumination. We then followed a matrix-based approach, similar to the one used in MoM, to solve for the weights of these dipole moments. However, since the radii of the spheres used to model the wire is determined by its radius, the number of unknowns and the size of the DM matrix typically is much larger than the corresponding size of

the matrix in MoM. To improve the numerical efficiency of DM, we discussed the use of high-level basis functions, or macro basis functions in Chapter 2. In particular, we explained a procedure to derive a set of entire domain macro basis functions, referred to as the Characteristic Basis Functions, which serve not only to reduce the size of the DM matrix, but also to ensure that the reduced matrix is well-conditioned.

Next, we used a combination of the DM method and the CBFs for the analysis of the doubly infinite FSS in Chapter 3. The numerical technique detailed in that chapter leveraged two fundamental principles to aid the analysis procedure. The principle of translational invariance allowed us to argue that the CBFs that are required to describe the current distribution on the element in the unit cell of the FSS are sufficient to completely describe the same on any other cell, except for a phase shift that is dictated by the direction of the incident plane wave. Once we find the induced current on a typical element of the FSS, we invoked the reciprocity principle to express the reflection coefficient of the FSS, as a ratio of the reaction of a suitably-defined field over that current, and the reaction of the same field over the currents on a PEC plate. The advantage of this approach to compute the reflection coefficient is that it circumvents the integration involved in computing the far-field radiated by the current induced on the FSS. We demonstrated that our numerical technique is general by analyzing not only planar but also non-planar FSSs that may be excited by an obliquely incident plane wave, in general. In contrast, the MoM code-2 can handle only planar FSSs, while the MoM code-1 can generate results only when the direction of the incident wave is close to the normal. It is noteworthy that the number of unknowns in our numerical code (the number of CBFs), are significantly lesser than those required in the commercially available codes. We have applied our numerical technique for wire type of PEC elements, and further work is required to extend this technique to be able to handle elements that involve a combination of PEC and dielectric bodies.

Bibliography

- [1] R. Harrington, *Field computation by moment methods*. Wiley-IEEE Press, 1993.
- [2] C. Klein and R. Mittra, “The effect of different testing functions in the moment method solution of thin-wire antenna problems,” *IEEE Transactions on Antennas and Propagation*, vol. 23, pp. 258–261, 1975.
- [3] C. Balanis, *Advanced engineering electromagnetics*. Wiley New York, 1989.
- [4] S. Wandzura, “Optimality of Galerkin method for scattering computations,” *Microwave and Optical Technology Letters*, vol. 4, no. 5, pp. 199–200, 1991.
- [5] H. Pocklington, “Electrical oscillations in wires,” in *Proc. Camb. Phil. Soc*, vol. 9, no. Part 7, 1897, pp. 324–332.
- [6] G. Thiele, “Wire antennas,” *Computer Techniques for Electromagnetics*, 1973.
- [7] S. Jarvenpaa, M. Taskinen, and P. Yla-Oijala, “Singularity extraction technique for integral equation methods with higher order basis functions on plane triangles and tetrahedra,” *International Journal for Numerical Methods in Engineering*, vol. 58, no. 8, pp. 1149–1165, 2003.
- [8] A. Howard Jr and D. Seidel, “Singularity extraction in kernel functions in closed region problems,” *Radio Science*, vol. 13, pp. 425–429, 1978.

- [9] Y. Rahmat-Samii, “On the Question of Computation of the Dyadic Green’s Function at the Source Region in Waveguides and Cavities (Short Papers),” *IEEE Transactions on Microwave Theory and Techniques*, vol. 23, no. 9, pp. 762–765, 1975.
- [10] J. Jackson, *Classical Electrodynamics*. John Wiley & Sons Inc, 1975.
- [11] R. Mittra, K. Panayappan, C. Pelletti, and A. Monorchio, “A universal dipole-moment-based approach for formulating MoM-type problems without the use of Green’s functions,” in *Proceedings of the Fourth European Conference on Antennas and Propagation (EuCAP)*, 2010, pp. 1–3.
- [12] R. Harrington, *Time-harmonic electromagnetic fields*. IEEE Press, 2001.
- [13] J. Bringuier, “Multi-scale techniques in Computational Electromagnetics,” Ph.D. dissertation, The Pennsylvania State University, 2010.
- [14] K. Yee, “Numerical solution of initial boundary value problems involving maxwell’s equations in isotropic media,” *IEEE Transactions on antennas and propagation*, vol. 14, no. 3, pp. 302–307, 1966.
- [15] K. Panayappan, J. Bringuier, R. Mittra, K. Yoo, and N. Mehta, “A New-Dipole-Moment based MoM Approach for Solving Electromagnetic Radiation and Scattering Problems,” in *USNC/URSI National Radio Science Meeting*, 2009.
- [16] S. Rao, D. Wilton, and A. Glisson, “Electromagnetic scattering by surfaces of arbitrary shape,” *IEEE Transactions on Antennas and Propagation*, vol. 30, no. 3, pp. 409–418, 1982.
- [17] R. Mittra and K. Du, “Characteristic basis function method for iteration-free solution of large method of moments problems,” *Progress In Electromagnetics Research*, vol. 6, pp. 307–336, 2008.

- [18] J. Pendry, A. Holden, D. Robbins, and W. Stewart, "Magnetism from conductors and enhanced nonlinear phenomena," *IEEE transactions on microwave theory and techniques*, vol. 47, no. 11, pp. 2075–2084, 1999.
- [19] B. Wu, W. Wang, J. Pacheco, X. Chen, T. Grzegorzczuk, and J. Kong, "A study of using metamaterials as antenna substrate to enhance gain," *Progress In Electromagnetics Research*, vol. 51, pp. 295–328, 2005.
- [20] J. Matson and F. O’Nians, "Antenna Feed System simultaneously operable at two frequencies utilizing polarization independent frequency selective intermediate reflector," 1966, uS Patent 3,231,892.
- [21] R. Ulrich, "Far-infrared properties of metallic mesh and its complementary structure," *Infrared Physics*, vol. 7, no. 1, pp. 37–55, 1967.
- [22] M. Dorschlag and T. DeTemple, "Far-IR optical properties of freestanding and dielectrically backed metal meshes," *Applied Optics*, vol. 20, no. 7, pp. 1245–1253, 1981.
- [23] R. Mittra, C. Chan, and T. Cwik, "Techniques for analyzing frequency selective surfaces-a review," in *IEEE Proceedings*, vol. 76, 1988, pp. 1593–1615.
- [24] P. Ewald, "Evaluation of optical and electrostatic lattice potentials," *Ann. Phys. Leipzig*, vol. 64, pp. 253–287, 1921.
- [25] I. Stevanovic, P. Crespo-Valero, K. Blagovic, F. Bongard, and J. Mosig, "Integral-equation analysis of 3-D metallic objects arranged in 2-D lattices using the Ewald transformation," *IEEE Transactions on Microwave Theory and Techniques*, vol. 54, no. 10, pp. 3688–3697, 2006.
- [26] A. Rashidi, private communication.

- [27] K. Yoo and R. Mittra, “A Novel Technique for Analysis of Periodic Structures Including EBGs,” in *IEEE Antennas and Propagation Society International Symposium*, 2010, to be published.